ANL-80-93

MATERIALS TECHNOLOGY FOR COAL-CONVERSION PROCESSES.

Progress Report for April—June 1980

ARGONNE NATIONAL LABORATORY

ARGONNE NATIONAL LABORATORY, ARGONNE, ILLINOIS

Prepared for the Office of Fossil Energy
U. S. DEPARTMENT OF ENERGY
under Contract W-31-109-Eng-38

Distribution Categories:
Coal Conversion and Utilization:
Coal Gasification (UC-90c)
Direct Combustion of Coal (UC-90e)
Materials and Components (UC-90h)

ANL-80-93

ARGONNE NATIONAL LABORATORY
9700 South Cass Avenue
Argonne, Illinois 60439

MATERIALS TECHNOLOGY FOR COAL-CONVERSION PROCESSES

Progress Report for
April—June 1980

William A. Ellingson
Program Manager

Materials Science Division

October 1980

Most recent reports in this series

ANL-79-56	January—March 1979
ANL-79-93	April—June 1979
ANL-80-12	July—December 1979
ANL-80-46	January—March 1980

TABLE OF CONTENTS

TABLE OF CONTENTS (continued)

LIST OF TABLES

LIST OF FIGURES

LIST OF FIGURES (continued)

LIST OF FIGURES (continued)

MATERIALS TECHNOLOGY FOR COAL-CONVERSION PROCESSES
Progress Report for
April-June 1980

HIGHLIGHTS

Task A -- Evaluation of Ceramic Refractories for Slagging Gasifiers *(C.R. Kennedy, S.W. Kreis, and R.J. Fousek)*

The twelfth 500-h test run in the slag-refractory test facility has been completed. Of the 16 different water-cooled refractories exposed to a high-iron oxide acidic coal slag (B/A = 0.55) at 1575°C, a fused-cast, chrome-spinel (80% Cr_2O_3) refractory was found to exhibit the highest corrosion resistance. As in the tests with other acidic and basic slags, high chromia content and high density were identified as important factors in minimizing the corrosion.

Task B -- Development and Application of Nondestructive Evaluation Methods for Coal-conversion Processes *(W.A. Ellingson, C.A. Youngdahl, and D. Wilson)*

Results of high-temperature erosion scanning at the Solvent Refined Coal (SRC) liquefaction plant in Tacoma, WA indicate low erosion rates which may be limited by the presence of an acoustically transparent reaction film composed of Cr, Fe, S and O. Special, extra-long 1.3-m (4-ft.) waveguides are being designed to supplement existing equipment for monitoring preheater-coil erosion rates at SRC. Results of ultrasonic inspection of the HYGAS high-pressure cyclone separator suggest that use of the cyclone should be terminated. A dedicated automatic data-acquisition system for the joint Exxon-ANL erosion program at Baytown, TX is in the final design stage. Recent results at the Morgantown Energy Technology Center have shown that acoustic correction for a through-the-wall thermal gradient can be made: This reduced the data scatter to < ±0.051 mm (±2 mil) and revealed incremental wear steps. Passive acoustic detection of internal liquid leaks past blockage valves seems possible through use of low-velocity mass-flow measuring methods. The observation that laminar and turbulent flow conditions can be present during leakage suggests that low-velocity flow can be detected through use of an ultrasonic cross-correlation flowmeter or a strain-sensitive method of detecting an impact pressure pulse. These two methods seem to hold promise for quantitatively measuring leakage flow of liquids past valves.

Task C -- Corrosion Behavior of Materials in Coal-conversion Processes *(K. Natesan and T. C. Tiearney*)*

Research on metallic corrosion in coal-gasification atmospheres has primarily involved testing in high-Btu pilot plants or laboratory simulations thereof, although the near-term economic feasibility of low-Btu processes in combined-cycle electric-power production appears promising. Consequently, information on the operating parameters (vessel pressures, gas compositions, and maximum temperatures) for eleven low-Btu gasifiers was analyzed to characterize the gaseous environments in terms of the oxygen, sulfur, and

*Visiting Appointee from Exxon Research and Engineering Company.

carbon potentials in these systems. In general, the product gas from low-Btu gasifiers exhibits lower oxygen potentials than that from high-Btu gasifiers. Sulfur is a more important corrodant than carbon in these environments. A comparison of the environments in various high- and low-Btu processes shows that even the conventional high-chromium alloys, such as Type 310 stainless steel and Incoloy 800, will undergo a sulfide mode of attack in nearly all low-Btu atmospheres, regardless of the sulfur content of the coal feedstock.

The results also show that there exists a threshold in oxygen partial pressure above which a continuous protective oxide scale is developed on the alloys. At 1144 and 923 K, these threshold oxygen partial pressures are, respectively, $\sim 10^3$ and $\sim 10^5$ times the oxygen partial pressure for the Cr oxide/Cr sulfide equilibrium. The analysis of the process environments and the experimental evidence clearly shows that novel design approaches and alternate materials are needed for effective utilization of coal via low-Btu gasification schemes.

Task D -- Erosion Behavior of Materials in Coal-conversion Processes *(J.Y. Park and W.J. Shack)*

A 24-h erosion-corrosion calibration test was performed on 1015 carbon steel, Type 304 SS, Incoloy 800, RA310 SS, and Stellite 6B in a simulated gasifier atmosphere (18 CO, 12 CO_2, 5 CH_4, 24 H_2, 39 H_2O, 1 NH_3, 1 H_2S in vol. %) at 816°C, using 150-μm alumina particles at an impingement velocity of 22 m/s and angles ranging from 16 to 81°. The erosion rates calculated from weight loss are in the range of 0.0-0.1 mg/g. A duplicating room-temperature erosion calibration test was performed. The results were in good agreement with the previous test results.

Task E -- Failure Analysis *(D.R. Diercks, J.Y.N. Wang, and G.M. Dragel)*

Four of the seven experimental thermowells prepared for trial exposure in the IGT U-GAS Pilot Plant have been exposed for a total of four plant runs on high-sulfur coal. No significant degradation of the four thermowells has been observed after these four runs. The examination of a failed internal solids transfer line from the IGT HYGAS Pilot Plant has been completed, and failure has been attributed to severe localized sulfidation of the high-nickel Inconel 182 weld metal used to fabricate the line. Thermodynamic data supporting this conclusion are presented. Failure of a thermocouple assembly from the same plant has been attributed to the presence of preexisting flaws in the wall of the Type 310 stainless steel sheath. These flaws permitted the coal-gasifier environment to come in contact with the interior of the thermocouple assembly, thereby causing a conversion of the MgO insulation to the less-dense $Mg(OH)_2$ and also leading to sulfide attack at the ID of the sheath.

A summary of the more important failure analyses performed on components from coal-gasification pilot plants over the past six years has been prepared, and is included in tabular form in the present report.

MATERIALS TECHNOLOGY FOR COAL-CONVERSION PROCESSES
Progress Report for
April-June 1980

FOREWORD

This materials engineering program, begun in 1974, includes studies on ceramic (refractory) and metallic materials presently being used or intended for use in coal-conversion processes. The program entails research in the fields of nondestructive testing and failure analysis, together with studies of erosive wear, corrosion, and refractory degradation. Appropriate laboratory and field experiments are integrated such that the results have impact on present pilot- and demonstration-plant and proposed full-scale designs. This report presents the technical accomplishments of the program for the period April-June 1980.

ABSTRACT

During this reporting period, the twelfth 500-h slag-refractory test run, which involved a high-iron-content acidic coal slag, was completed. High chromia content and high density were again identified as important factors in minimizing corrosion of refractories.

Results from the high-temperature nondestructive erosion-scanner installation at the Solvent Refined Coal plant has revealed the presence of a hard film composed of Cr, Fe, S and O_2, which seems to reduce erosive wear but is acoustically transparent. Further improvements in the erosion-scanner data-acquisition system through employment of a correction for through-wall thermal gradients have reduced data scatter to $< \pm 0.05$ mm. Quantitative detection of internal liquid leaks past critical valves in coal liquefaction plants seems possible through use of low-velocity ultrasonic or strain-sensitive flowmeters together with passive acoustic systems.

Studies of high-temperature gaseous corrosion in low-Btu environments show that the potential exists for sulfide attack even in high-chromium alloys such as 310 SS. Recent results show that the oxygen partial pressure threshold above which a protective oxide film forms is 10^3 to 10^5 (at 1144 and 923 K, respectively) times the oxygen partial pressure for Cr oxide/Cr sulfide equilibrium.

Four of the seven special thermowells installed at IGT's U-gas plant have shown no significant degradation after an additional 500-h run. Further runs are planned to allow more hours of exposure.

Failure-analysis activities this period included analysis of a failed internal transfer line and a thermocouple sheath, both from the HYGAS coal-gasification pilot plant. A complete summary of the more important coal-gasification failures analyzed at Argonne is included in this report.

INTRODUCTION

Economical, reliable, and safe conversion of coal into clean and usable alternate fuels will be advanced through the use of durable materials of construction. The technical information base applicable to the behavior of materials in the operating environments characteristic of various coal-conversion processes is extremely limited. Hence, reliable materials selection and lifetime prediction are difficult to achieve. This program is designed to provide part of the materials information necessary for successful operation of coal-conversion systems. The present report is the twenty-first progress report submitted by ANL to the Office of Advanced Research and Technology, Office of Fossil Energy under Project Number 7106, "Materials Technology for Coal-conversion Processes".

The project includes five tasks: (A) Evaluation of refractories exposed to coal slag under conditions typical of those encountered in slagging gasification processes; (B) development and application of nondestructive evaluation methods; (C) evaluation of the corrosion behavior of commercial alloys; (D) development of analytical models to predict the erosive-wear behavior of materials; and (E) analysis of failed coal-conversion plant components.

Task A -- Evaluation of Ceramic Refractories for Slagging Gasifiers
(C. R. Kennedy, S. W. Kreis, and R. J. Fousek)

Test run 12 has been completed. In this test, 16 different water-cooled refractories were exposed to a synthetic high-iron oxide acidic coal slag (see Table I for composition). In most cases, one full-length (228 mm) and one half-length refractory brick was tested. Although several shutdowns of the furnace occurred, the plenum temperature was maintained at ∿1575°C for a total of 493 h with a partial pressure of oxygen $\sim 10^{-2}$ to 10^{-4} Pa (determined by calculations based on chemical analysis of gas samples) throughout the test. As measured with an optical pyrometer, the hot-face temperature of the full-length refractory number 260 was ∿1520°C.

As previously reported,[1] two carbon-impregnated refractories were badly corroded after only 36 h. These refractories were removed from the unit and replaced with two additional samples of number 260 alumina-chromia refractories (no quantitative data were taken on these bricks). After the test was terminated, the refractories were removed from the vessel and sectioned along the vertical midplane so that the depth of corrosion and penetration could be measured. The cut sections are shown in Figs. 1 and 2. Tables II and III detail the relative corrosion resistance of these refractories. Nonuniform corrosion of four bricks [numbers 86 (1/2-length), 16 (full-length), 100 (full-length), and 400 (full-length)] was observed, and was attributed to inaccurate positioning, i.e., hot faces not at right angles to the radii of the slag bath. This made the measurements of the depth of removal and penetration difficult to evaluate in these cases. Therefore, for these bricks, the maximum and minimum values of the depth of removal have been presented in parentheses, along with a weighted average value.

As observed in previous tests with less acidic slags of low iron oxide content, dense high-chromia refractories performed the best. The fused-cast chrome-spinel (number 22) and alumina-chromia (numbers 280 and 38) were clearly superior to the others tested. For alumina-chromia refractories, as the chromia content increased from 7 to 32%, the corrosion decreased substantially. The pure alumina fused-cast refractory (number 2) was only about as good as the sintered alumina-10% chromia refractory (number 16), despite the significantly lower porosity of number 2 (1-2% versus 16-18%). The two magnesia-chrome refractories (numbers 400 and 41) were intermediate in corrosion resistance; number 400, with a higher chrome and lower magnesia content, clearly outperformed number 41. As detailed in Table IV, most of the refractories exhibited some degree of cracking, which in most cases can be attributed to thermal stress. Full-length samples of numbers 100, 260, and 280 were completely fractured, with the fracture plane parallel to and 35 mm from the hot face. In general, the magnesia-chrome and chemically bonded alumina-chromia plastic products were less cracked than the other refractories, and the dense high-chromia refractories were extensively cracked.

Metallographic and SEM examinations of selected refractories from this test will be performed in upcoming quarters.

TABLE I. Slag Composition during Test Run 12

Component	Exposure Time,[a] h		
	123	391	485
SiO_2 (S)	44.8	44.9	44.0
Al_2O_3 (A)	18.8	17.8	19.6
Fe_2O_3 (F_1)	1.0	0.9	1.8
FeO (F_2)	18.7	18.1	17.3
Fe (F_3)	0.4	0.6	0.5
CaO (C)	9.2	10.9	10.2
MgO (M)	3.0	3.0	2.9
Na_2O (N)	1.4	1.2	1.1
K_2O (K)	1.6	1.4	1.3
TiO_2 (T)	0.9	0.9	0.9
Other	0.2	0.3	0.4
B/A Ratio[b]	0.55	0.57	0.54
Ferritic Content,[c] %	4.0	4.0	8.0

[a] Time at 1575°C.

[b] Base-to-acid ratio $B/A = \dfrac{(F_1 + F_2 + F_3 + C + M + N + K)}{(S + A + T)}$.

[c] Ferritic content $= \dfrac{\text{wt \% } (Fe_2O_3)}{\text{wt \% } (Fe_2O_3) + 1.11 \text{ wt \% } (FeO) + 1.43 \text{ wt \% } (Fe)}$.

TABLE II. Relative Corrosion Resistance of Chemically Bonded and Sintered Refractories Exposed to a High-Iron Oxide Acidic Coal Slag at 1575°C for 493 h

Number	Type	Composition, wt %	Average Depth of Removal,[a] mm		Average Depth of Penetration,[a] mm	
			Full-length	1/2-length	Full-length	1/2-length
86	Chemically bonded alumina-chromia plastic	Al_2O_3(84.5)-Cr_2O_3(10.5)-SiO_2(0.2)-P_2O_5(4.6)	38	16 (11-21)	63	37
190	Sintered alumina-chromia	Al_2O_3(92)-Cr_2O_3(7.5)-SiO_2(0.5)	18	15	28	23
16	Sintered alumina-chromia	Al_2O_3(89.7)-Cr_2O_3(10)	17 (12-18)	11	28	14
100	Sintered alumina-chromia	Al_2O_3(89)-Cr_2O_3(10)	16 (7-25)	9	27	17
852	Sintered alumina-chromia	Al_2O_3(81.1)-Cr_2O_3(16.6)-P_2O_5(0.8)-SiO_2(0.5)-Fe_2O_3(0.5)-Na_2O(0.5)	NT[b]	7	NT	17
109	Chemically bonded alumina-chromia plastic	Al_2O_3(67)-Cr_2O_3(32)-P_2O_5(1)	10	6	30	10
260	Sintered alumina-chromia	Al_2O_3(67)-Cr_2O_3(32)	10	6	ND[c]	ND
40	Sintered magnesia-chromia	MgO(61)-Cr_2O_3(19)-Fe_2O_3(11)-Al_2O_3(6)-SiO_2(1)-CaO(2)	NT	11	NT	14
41	Sintered magnesia-chromia	MgO(55)-Cr_2O_3(20)-Al_2O_3(8)-FeO(11)-SiO_2(2.5)-CaO(0.5)-TiO_2(1.5)	23	NT	27	NT
400	Sintered magnesia-chromia	MgO(41.6)-Cr_2O_3(27.1)-Al_2O_3(13.3)-Fe_2O_3(15.9)-CaO(0.5)-SiO_2(1.2)	14 (11-19)	NT	18	NT
505	Carbon impregnated alumina-chromia	Al_2O_3(52.5)-Cr_2O_3(20.6)-C(9.1)-Si(9.6)-P_2O_5(2.8)-SiO_2(4.1)	E[d]	NT	ND	NT
506	Carbon impregnated alumina-chromia	Al_2O_3(38.1)-Cr_2O_3(25.2)-C(17.9)-Si(9.4)-SiO_2(8.2)	E	NT	ND	NT

[a]Measured from the original hot face.

[b]NT = not tested.

[c]ND = not possible to determine.

[d]E = removed after 36 h because of extreme corrosion.

TABLE III. Relative Corrosion Resistance of Fused-cast Refractories Exposed to a High-Iron Oxide Acidic Coal Slag at 1575°C for 493 h

Number	Type	Composition, wt %	Average Depth of Removal,[a] mm		Average Depth of Penetration,[a] mm	
			Full-length	1/2-length	Full-length	1/2-length
2	Alumina	Al_2O_3(99)-Na_2O(0.5)	18	8	24	11
22	Chrome-spinel	Cr_2O_3(80)-MgO(8)-Fe_2O_3(6)-Al_2O_3(5)-SiO_2(1)	3	3	4	4
38	Alumina-chromia	Al_2O_3(60)-Cr_2O_3(27)-MgO(6)-Fe_2O_3(4)-SiO_2(2)	7	4	9	5
280	Alumina-chromia	Al_2O_3(65)-Cr_2O_3(32)-FeO(1)-CaO(0.6)-MgO(0.6)	5	4	7	5

[a]Measured from the original hot face.

TABLE IV. Qualitative Posttest Observations of Refractories in Test Run 12

Number	Length[a]	Comment
86	Full, 1/2	Intact, but pronounced swelling and pitting above slag line
190	Full, 1/2	Small cracks but intact, slight pitting above slag line
16	Full	Cracked, bottom section fractured during removal from test vessel, slight pitting above slag line
	1/2	Small cracks but intact
100	Full	Fractured parallel to hot face
	1/2	Small cracks but intact
852	1/2	Small cracks but intact
109	Full, 1/2	Intact, slight pitting above slag line
260	Full	One sample cracked but intact, one fractured parallel to hot face
	1/2	One sample intact, one cracked but intact
41	Full, 1/2	Small cracks but intact, severe pitting above the slag line
400	Full	Small cracks but intact, severe pitting above the slag line
2	Full, 1/2	Small cracks but intact
22	Full, 1/2	Cracked but intact
38	Full, 1/2	Cracked but intact
280	Full	Fractured parallel to hot face
	1/2	Cracked but intact

[a] Full length = 228 mm; 1/2-length = 114 mm.

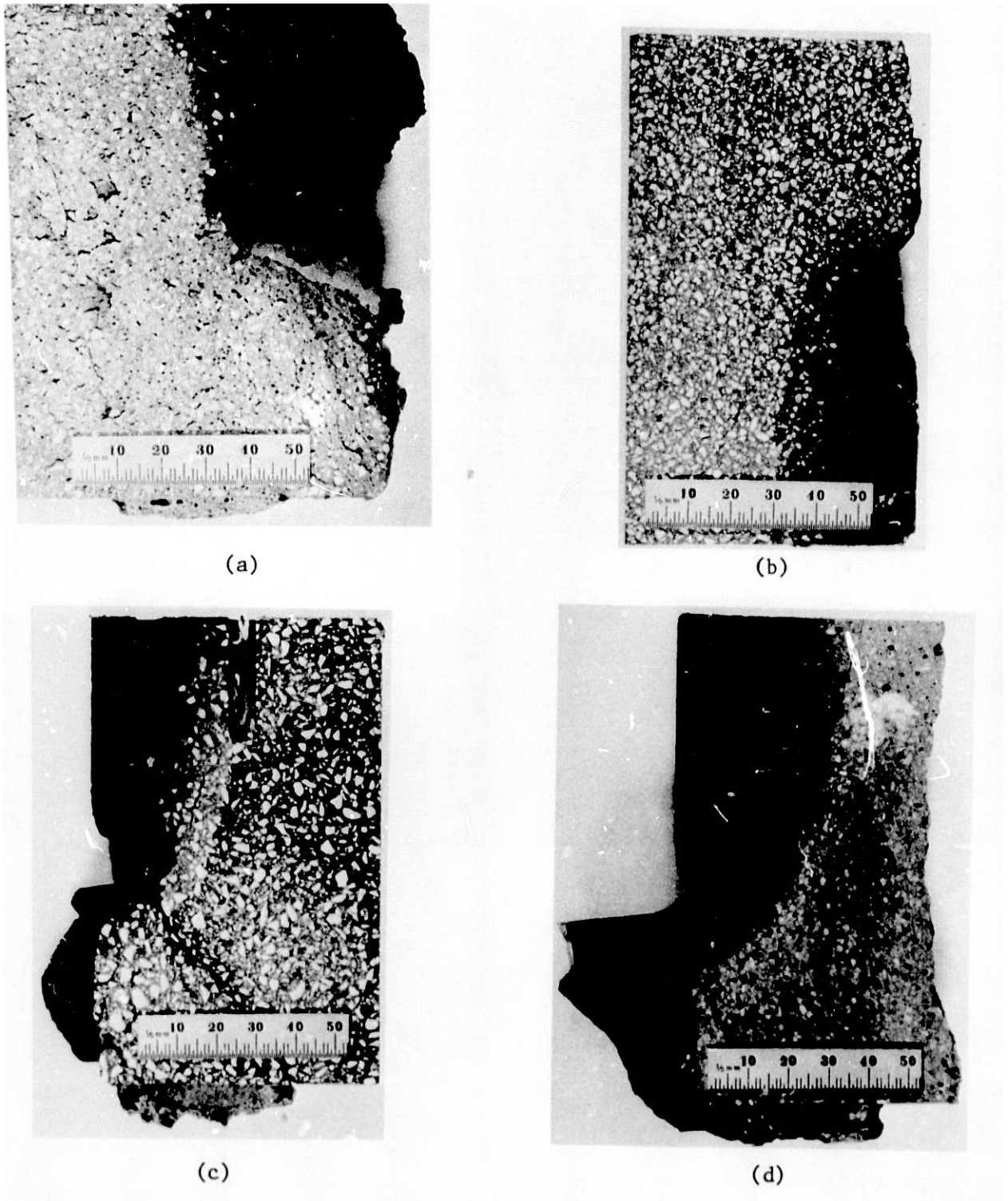

Fig. 1. Cut Sections of Full-length Refractories Exposed to a High-Iron Oxide Acidic Coal Slag in Test Run 12. Number (a) 86, (b) 190, (c) 16, (d) 100, (e) 109, (f) 260, (g) 41, (h) 400, (i) 2, (j) 22, (k) 38, and (l) 280. The right-hand vertical face of a,b,f,g, and h and the left-hand vertical face of the other specimens were exposed to the slag. Note that the entire length of each brick is not shown.

(e)

(f)

(g)

(h)

Fig. 1 (contd.)

(i)

(j)

(k)

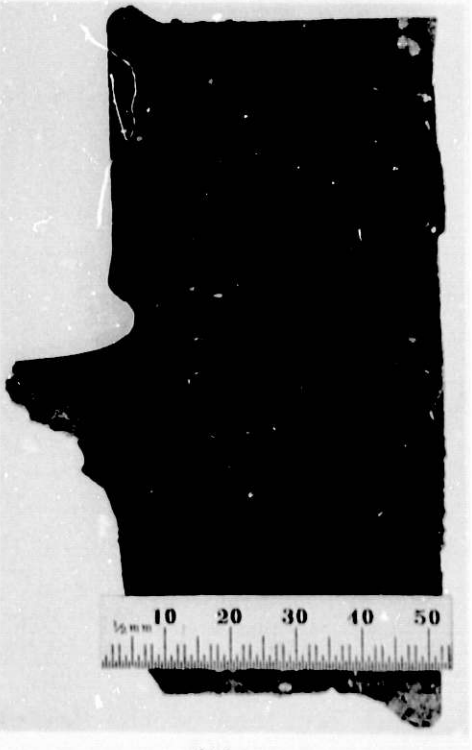

(l)

Fig. 1 (contd.)

(a)

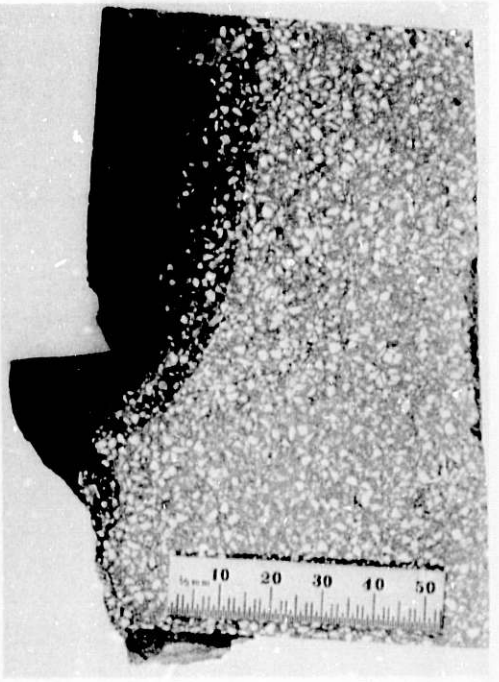

(b)

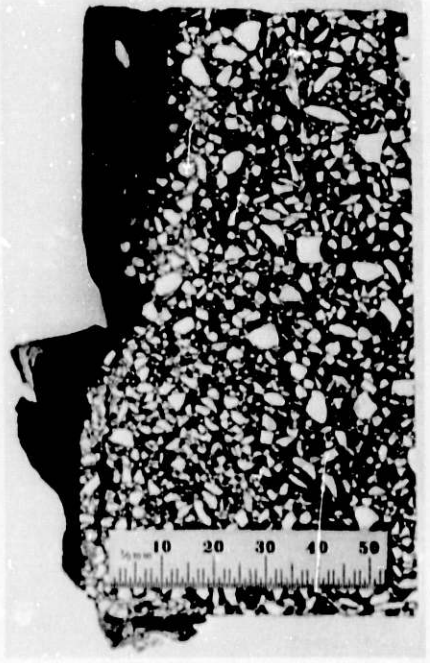

(c)

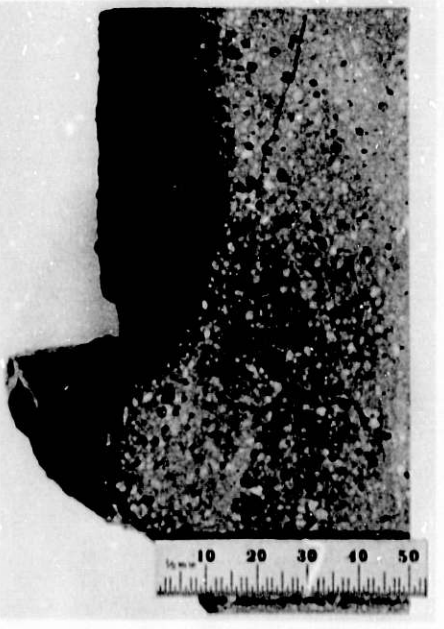

(d)

Fig. 2. Cut Sections of the Half-length Refractories Exposed to a High-Iron Oxide Acidic Coal Slag in Test Run 12. Number (a) 86, (b) 190, (c) 16, (d) 100, (e) 852, (f) 109, (g) 260, (n) 40, (i) 2, (j) 22, (k) 38, and (l) 280. With the exception of h, the left-hand vertical face of each specimen was exposed to the slag. Note that the entire length of each brick is not shown.

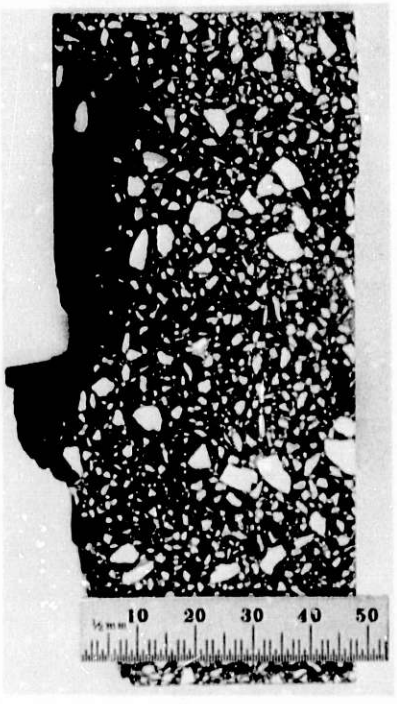

(e)

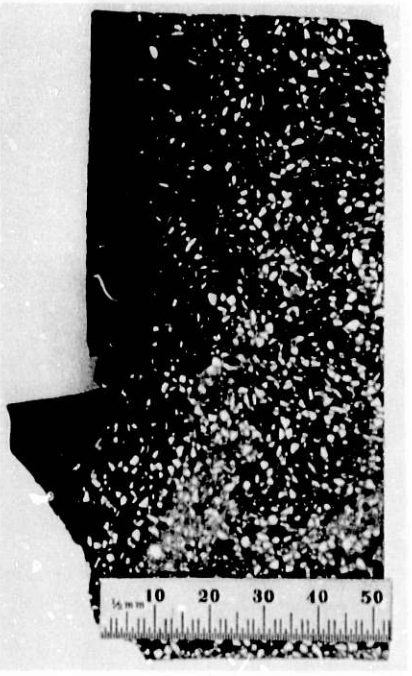

(f)

(g)

(h)

Fig. 2 (contd.)

(i)

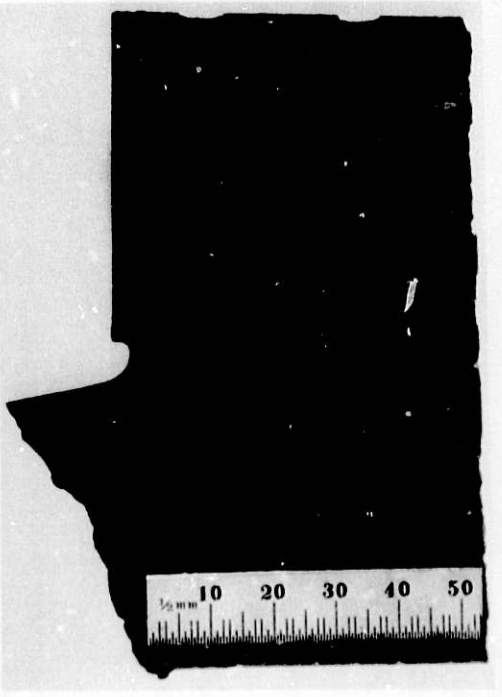

(j)

(k)

(l)

Fig. 2 (contd.)

Task B -- Development and Application of Nondestructive Evaluation Methods for Coal-conversion Processes *(W.A. Ellingson, C.A. Youngdahl, and D. Wilson)*

1. Erosive Wear: Detection and Monitoring

a. Metallic Transfer Lines

(1) Ultrasonic Studies - Pilot Plants

(a) Solvent Refined Coal Liquefaction Plant

A plant visit was made in May 1980 to participate in (1) data-verification work pertinent to erosive wear of the coal liquefaction process piping, and (2) planning the application of the ANL erosion scanner[1,2], currently in operation at the plant, to new components of the process piping.

Results obtained during the visit include those shown in Table V. The low rate of wear evident in Table V may be associated with a fine particle size distribution (not yet elucidated) in the slurry and with the presumed presence of a reaction film, as noted in the previous report.[1]

An initial analysis by ANL of a sample of such film on Type 347 SS piping used at the SRC pilot plant revealed the presence of chromium, iron, sulfur, and oxygen as the major constituents (concentrations of carbon and nickel were not substantial). The film resists removal by grinding but has been removed with difficulty by glass-bead blasting as described in Ref. 3. Ultrasound is readily transmitted by the film, and the wall-thickness data probably include a film effect. However, the film within piping monitored by the ANL scanner is thought to be very thin. Removal of a section of piping is planned during the next quarter to examine any reaction film that may be present.

Currently, additional waveguides are being fabricated for application to new pilot-plant piping in September, and design improvements are being incorporated in long waveguides for use in the slurry preheater. Auxiliary control circuits are being prepared to (1) accommodate various waveguide lengths, and (2) permit the setting of an optimal threshold level of the automatic gain control for each channel of the scanner.

(b) Morgantown Energy Technology Center Fixed-bed Gasifier

Figure 3 shows cyclone-wear data reduced from the strip-chart recording of the ANL erosion scanner during the November-December 1979 run of the fixed-bed gasifier at the Morgantown Energy Technology Center (METC), which were briefly noted in the previous report.[1] The whole distances from the shoulder of waveguide no. 17, the site of greatest wear, to the eroding surface of the Type 316 SS high-temperature effluent cyclone are given in the figure in order to illustrate the small magnitude of the percentage of scatter error in the reduced results.

To achieve this reduction of scatter, an additional data-reduction step was applied beyond those discussed in Ref. 2: Errors from a varying thermal gradient between the waveguide shoulder and the eroding surface were

TABLE V. Changes in Ultrasonically Indicated Wall Thickness at Waveguide Sites[a] on Process-line Piping at SRC Pilot Plant, from mid-January 1980 to mid-May 1980

Waveguide No.	Change, mils[b]	Waveguide No.	Change, mils[b]
1	-1	16	-1
2	-3	17	-1
3	-3	19	-1
4	-3	20	-1
5	-3	22	(+1)
6	-3	23	0
7	0	24	0
8	-1	26	-1
9	-2	27	-1
10	-2	28	-2
11	-2	29	(+2)
12	0	30	(+1)

[a]The present wall-thickness changes are in addition to changes caused by previous operation and reported in Ref. 1. Locations of waveguides were described in Ref. 2.

[b]1 mil = 0.001 in. = 0.0254 mm.

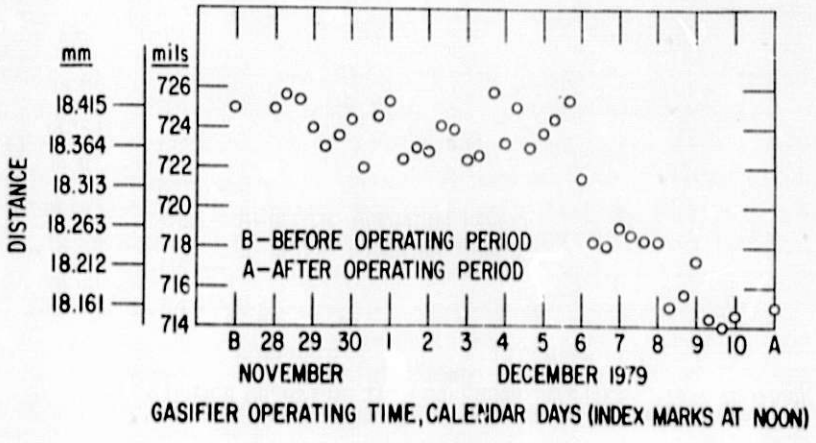

Fig. 3. Wear of Type 316 SS High-temperature Effluent Cyclone at METC During Gasifier Operation. Ultrasonically measured distances from shoulder of waveguide no. 17 (the site of greatest wear) to eroding surface were corrected as described in the text and plotted vs gasifier operating time; 304 SS calibration was used.

removed by reference to contemporaneous results from a site (waveguide no. 9) at which the cyclone was not measurably eroded during the run, according to data obtained at ambient temperature before and after the run. In addition to reducing scatter, this approach resulted in good agreement between elevated-temperature data for waveguide no. 17 and ambient-temperature measurements made before and after the run (Fig. 3).

The improved results of Fig. 3 reveal that the wear occurred primarily during specific, relatively brief periods within the run. Data from the pilot plant show that the first period of increased wear rate coincides with a peak in flow velocity and that the second coincides with the system "burn-out" step performed near the end of the plant run. However, two additional peaks in the flow velocity did not produce high rates of wear; distinctions between the conditions accompanying these velocity peaks and the above-mentioned one are being sought.

In July, two small carbon steel tar-separator cyclones will be instrumented with seven acoustic waveguides each, in preparation for plant operations expected to begin in August. These new erosion-monitoring sites will be incorporated in the scanner system previously provided by ANL to METC.

A collaborative paper, "Erosive Wear and Design Evaluation of a Stainless Steel Cyclone on the Coal Gasification Pilot Facility at Morgantown" by C.A. Youngdahl (ANL), K. Pater (METC), and M.J. Gorski (TRW Energy Systems Group), has been submitted for presentation at the Conference on Properties and Performance of Materials in the Coal Gasification Environment (Pittsburgh, PA, September 8-10, 1980).

(c) HYGAS High-pressure Cyclone Separator

The HYGAS stainless steel cyclone[2] was surveyed by ultrasonic and gamma-ray methods in mid-April and early June 1980. Ultrasonic shear-wave techniques were used to examine the cyclone for possible stress-corrosion cracks; no significant cracks were found. Longitudinal-wave, pulse-echo techniques were used to survey those portions of the internally eroded pressure wall that had not already been reinforced with external sheaths. The zone of least remaining wall thickness, 13.5 mm (0.53 in.), was located on the cyclone body cylinder at the inlet centerline and near the inner plate of the inlet conduit. Gamma radiography revealed a second region of pronounced thinning below and near the weld between the upper and lower body cylinders: The remaining thickness in this area, determined ultrasonically, was 14.7 mm (0.58 in.). The thickness of these components before erosion was almost 23 mm (0.9 in.). HYGAS plans to terminate the use of this cyclone during the next quarter.

(d) Exxon Coal Liquefaction Pilot Plant (ECLP)

It is planned to field-test pressure-coupled acoustic waveguides[2] at six locations on the ECLP process system. Four or more waveguides will be employed at each of the sites, which were chosen by plant personnel as suspected erosion areas. The ANL erosion scanner[1,2] is being adapted to this application, and a small data-acquisition system dedicated to the scanner is being incorporated for automatic data reduction and printing of results.

Costs are being shared by Exxon and ANL. Installation of the system is scheduled for September.

2. Refractory Installation Practices

a. Detection of Thermally Induced Acoustic Emissions from Refractory Concrete Materials

Additional progress has been made this quarter on preparation of the state-of-the-art report. Also, a meeting was held with Hotworks Services, Inc. (Lexington, KY) to discuss implementation of acoustic-emission detection during dryout and cool-down of thick refractory linings. Agreements were reached for potential joint field tests with Hotworks.

3. Component Inspection

a. Acoustic Detection of Valve Leaks

Last quarter[1] it was reported that five valves had been selected for monitoring at the Exxon Donor Solvent Plant in Baytown, TX. During this quarter, additional work addressed the problem of quantifying the leakage rates by non-intrusive acoustic emission techniques.

Control-valve leak detection using acoustic emission techniques has recently received widespread attention, which has produced several successful methods.[4] Although detection is relatively straightforward, the correlation of the acoustic signal with mass-flow rate is considerably more complicated. The feasibility of using various active and passive mass-flow correlation techniques, with emphasis on low-velocity measurements, was reviewed during this quarter.

For liquids and slurries (e.g., coal-oil, coal-water) under non-choked flow conditions, passive measuring techniques alone are not feasible. This is due to lack of control and/or definition of the parameters affecting the acoustic signal, making empirical correlation of the internal flow rate impractical. Consequently, active measurement techniques for correlating mass flow with the detected acoustic signal present the only reasonable approach.

Owing to the nature of flow and fluid constraints, flow rates may be very low; this results in either laminar or turbulent conditions upstream of valves selected for leakage monitoring. Because of the associated low velocities, flowmeters based upon the Doppler principle would be expected to incur unacceptable errors.[5] For this reason, two alternate methods have been reviewed which might be expected to yield acceptable accuracies. These methods are described in the next two sections.

(1) Ultrasonic Cross-correlation Flowmeter

It has recently been recognized[6] that turbulent flow contains a coherent structure which is transported downstream at some fraction of the mean flow velocity, $\bar{v}$. If the coherent fluctuations are observed (e.g.,

optically or electronically) at two axial locations, some degree of correlation between these two observations will exist. The degree of correlation will be good if the period between observations is small relative to the time scale for turbulent decay.

A so-called ultrasonic cross-correlation flowmeter, based on the above principles, has recently been tested.[7] The basic technique involves diametrical transmission of two parallel ultrasonic beams separated by a distance L. Modulation in the amplitude and/or phase of the received pulse are detected as shown in Fig. 4. These modulations of the input pulse are due to the coherent turbulence in the flow, which produces local fluctuations in pressure and density. Proper demodulation and measurement of these changes and subsequent cross-correlation of the received signals has been shown to yield an estimate of the mean transit time, τ_m, of the disturbance. From this information, the average fluid velocity can be easily calculated by

$$\bar{v} = k \frac{L}{\tau_m} \quad , \tag{1}$$

where k is the velocity profile correction factor and L is the transducer spacing.

The cross-correlation function is given by

$$T_{xy}(\tau) = \lim_{T \to \infty} \frac{1}{T} \int_0^T x(t)y(t+\tau)dt \quad , \tag{2}$$

where x(t) and y(t+τ) represent the signal at A and B, respectively. Owing to the natural decay of the turbulent flow patterns between measurement points A and B, the signals may differ significantly. However, sufficient cross-correlation peaks have been shown to exist[8] so that acceptably accurate measurements of fluid velocity are possible.

This basic concept, which has been used successfully for turbulent flows, would not be applicable to a homogeneous isothermal laminar flow field, since no naturally occurring disturbance exists. However, for either coal-oil slurries or nonisothermal single-phase flows, the basic technique should be applicable. In fact, it is reasonable to expect that better cross-correlation, and hence increased accuracy, could be achieved for the latter case. This observation is based upon the characteristic time scales for laminar (molecular) diffusion vs turbulent diffusion of density and temperature fluctuations.

The ratio of the time scales can be inferred by dimensional analysis. First, consider the thermal diffusion equation, neglecting the laminar convection term given by

$$\frac{\partial T}{\partial t} = \alpha \nabla^2 T \quad . \tag{3}$$

Defining T_m, ΔT, and L as the molecular diffusion time scale, temperature difference, and characteristic length, respectively, yields

$$\frac{\Delta T}{T_m} \sim \alpha \frac{\Delta T}{L} \tag{4}$$

or

$$T_m \sim \frac{L^2}{\alpha} \quad . \tag{5}$$

Denoting the turbulent characteristic length scale and velocity scale as L and $\bar{u}$, respectively, yields the turbulent time scale

$$T_t \sim \frac{L}{\bar{u}} \quad . \tag{6}$$

Combining Eqs. (5) and (6) yields

$$\frac{T_t}{T_m} \sim \frac{\alpha}{\bar{u}\, L} = \frac{1}{P_e} \quad , \tag{7}$$

where P_e = Peclet number. Since $\alpha/\nu \sim 1$ for water, we find that

$$\frac{T_t}{T_m} \sim \frac{1}{R_e} \quad , \tag{8}$$

where R_e is the Reynolds number. Thus we would expect the laminar temperature fluctuation to remain coherent much longer than the corresponding turbulent fluctuations.

Although ultrasonic cross-correlation flowmeters for gas and liquid flows are similar in design, one subtle difference exists: For a liquid flow, it is more effective to employ amplitude modulation, whereas for a gas flow, phase modulation works best. The reason is that for liquids, the acoustic reflection coefficient is small; consequently, acoustic standing waves are weak. For example, if the two media are water and steel, the respective impedances, ρc, are 1.4×10^6 and 4.7×10^7 kg/m^2-s.[8] The transmission coefficient is about 0.1, which represents a loss of only 10 dB. If, however, the water is replaced by air, ρc = 400 kg/m^2-s. The loss becomes 60 dB, which represents a poor acoustic coupling. This then implies the possible existence of standing waves. Finally, as with the attenuating flowmeter, the frequency of the pulse should be above the background noise.

Considering the liquid system only, i.e., disregarding standing waves, the signal received by the transducer will be of the form

$$V = V_o e^{-\alpha \ell} \sin(\omega_c t) \quad , \tag{9}$$

where α = attenuation coefficient, ω_c = carrier frequency, and ℓ = length of the acoustic path, which will vary in time owing to the density fluctuations. In Eq. (9), the amplitude attenuation coefficient for ultrasonic waves in liquids is given by the Stokes-Kirchoff[9] expression:

$$\alpha = \frac{2\rho f^2}{\rho c^3} \left[\frac{4}{3}\mu + \frac{\gamma-1}{c_p} k \right] \quad . \tag{10}$$

In this expression, k is the thermal conductivity, μ the viscosity, c_p the specific heat, ρ the density, γ the ratio of specific heats, c the speed of sound, and f the frequency. From this expression, it is obvious that for high-frequency sound waves, the attenuation can be significant. In addition, and more importantly, the temperature gradient has an exponential effect on attenuation, since both μ and k are proportional to temperature.

In addition to changes in α due to temperature gradients, the distance ℓ in Eq. (9) is modified according to

$$\ell = \langle \ell \rangle \left(1 + \frac{\Delta \ell}{\ell}\right) \quad . \tag{11}$$

In this expression, $\langle \ell \rangle$ is the ensemble average and $\Delta \ell$ is the length variation due to density change.

The receiver signal is thus modulated by a voltage given by

$$V_1 = c_1 \left[\frac{1}{T} \int_o^T \overline{V}^2 dt \right]^{1/2} \quad , \tag{12}$$

where $\overline{V}$ is the amplitude modulation of V due to the variations in α and ℓ, and c_1 is a constant.

By cross-correlating this receiver signal, one can use the peak in $T_{xy}(\tau)$ to obtain the transit time τ_m of the temperature fluctuations between points A and B.

(2) Attenuating Flowmeter

The second technique proposed for accurately obtaining low fluid velocities involves measuring the sound attenuation of various mechanically induced vibratory modes (Fig. 5). In this method, both upstream and downstream wave-amplitude attenuation is determined from a high-frequency ($\gtrsim$ 100-kHz) tone burst, as shown schematically in Fig. 6. A high-frequency pulse is selected so as to avoid contamination by high-energy background acoustic emissions which are typically below 70 kHz.[2] In addition, pulse, as opposed to steady-state, excitation is proposed so that end reflections from the upstream and downstream wave will not affect the measurements.

The operation of such a system is as follows: A pressure pulse is generated by a sound source on the upstream side of an obstruction (e.g., valve, orifice plate, etc.). Strain gauges are mounted at equal distances upstream and downstream from the source. These gauges will detect the pulse

by measuring the pipe-wall response to the pressure wave. For the case of zero fluid velocity, the recorded pulses should be identical. Any difference due to material inhomogeneities can be compensated for through appropriate electronic circuit adjustments.

When the fluid in the pipe has a finite velocity, the pressure amplitude of the upstream wave will be larger than that of the downstream wave and the ratio will increase monotonically with fluid velocity. Accurate measurement of this amplitude ratio would provide a simple correlation for the average fluid velocity. The theoretical basis for this amplitude variation, along with the technique for separating the mechanically induced vibratory modes, will be outlined next.

Sound propagation inside a duct is described by the solution of an eigenvalue equation, and the sound propagates in particular modes. The lowest mode propagates at all frequencies, while each higher mode propagates only above its cutoff frequency. Below this cutoff frequency, the mode is exponentially attenuated.[10] Thus, to accurately measure the attenuation from the sound source, measurement techniques that separate the sound field into the various modes are necessary.

The general characteristics of the first few modes can be inferred by looking at the solution to a highly idealized model. Considering an inviscid, isentropic, fully developed flow, the linearized Euler equations are

$$\frac{\partial v'_r}{\partial t} + V_o \frac{\partial v'_r}{\partial z} = -\frac{1}{\rho_o}\frac{\partial p'}{\partial r} \quad , \tag{13}$$

$$\frac{\partial v'_\theta}{\partial t} + V_o \frac{\partial v'_\theta}{\partial z} = -\frac{1}{\rho_o r}\frac{\partial p'}{\partial \theta} \quad , \tag{14}$$

$$\frac{\partial v'_z}{\partial t} + V_o \frac{\partial v'_z}{\partial z} + v'_r \frac{\partial V_o}{\partial r} = 0 \quad . \tag{15}$$

The general solution[11] can be written as

$$p'(\bar{r},\theta,\bar{z}) = \sum_m \sum_n C_{mn} R_{mn}(\bar{r}) \cos(m\theta + \phi_{mn}) e^{i(\omega t - k_{mn}\bar{z})} \quad .$$

From this solution, the pressure at the inner pipe wall at some axial locations becomes

$$\begin{aligned} p'(1,\theta,\bar{z}) = p_w(\theta) &= C_{00}\cos(\omega t - k_{00}\bar{z}_0) \\ &+ C_{10}\cos(\theta + \phi_{10})\cos(\omega t - k_{10}\bar{z}_0) \\ &+ C_{20}\cos(2\theta + \phi_{20})\cos(\omega t - k_{20}\bar{z}_0) \quad . \end{aligned} \tag{16}$$

From Eq. (16), the mean time-averaged pressure, $\overline{P}^2_{mn}$, can be determined. Performing the required operations yields

$$\overline{P}^2_{00} = \frac{1}{16}\overline{\left[P_w(0) + P_w(\tfrac{\pi}{2}) + P_w(\pi) + P_w(\tfrac{3\pi}{2})\right]^2} \quad , \tag{17}$$

$$\overline{P}^2_{10} = \frac{1}{4}\overline{\left[P_w(0) - P_w(\pi)\right]^2} \quad , \tag{18}$$

$$\overline{P}^2_{20} = \frac{1}{16}\overline{\left[P_w(0) + P_w(\pi) - P_w(\tfrac{\pi}{2}) - P_w(\tfrac{3\pi}{2})\right]^2} \quad , \tag{19}$$

at four circumferential locations separated by 90° intervals. The resulting pipe-wall deformations are shown in Fig. 5. The signals from the four circumferential strain gauges can then be separated by a similar technique described in Ref. 11. After the lowest modes have been separated, an accurate measurement of the attenuation should be possible.

Next, the physical mechanisms involved in attenuation of the acoustic-wave amplitude will be briefly outlined. Continuing to take a somewhat heuristic approach to the actual problem, we will consider first a constant-velocity (i.e., no velocity gradient), two-dimensional, inviscid isotropic analogue. For this situation, the wave equation is

$$\left(\frac{\partial}{\partial t} + v\frac{\partial}{\partial x}\right)^2 p = c^2\nabla^2 p \quad . \tag{20}$$

The plane-wave solution[9] is of the form

$$p = P_1 \cos(k_y y) e^{ik_x x} e^{i\omega t} \quad . \tag{21}$$

Applying rigid-wall boundary conditions yields the following expressions for the upstream and downstream attenuation factors, respectively:

$$\alpha_U = \frac{1}{2d(1 - M)^2} \quad ; \tag{22a}$$

$$\alpha_D = \frac{1}{2d(1 + M)^2} \quad . \tag{22b}$$

In these expressions, $M(\equiv \frac{v}{c})$ is the Mach number and d is the distance between the infinite parallel walls. From Eqs. (22a) and (22b), we obtain the pressure ratio of the upstream to downstream propagating wave,

$$\left| \frac{P_U}{P_D} \right| = \frac{(1+M)^2}{(1-M)^2} \quad . \tag{23}$$

Physically, this effect is simply related to the wavelength streching of the downstream wave and the corresponding compression of the upstream wave.

In addition to this effect, an attenuation occurs when the velocity contains a gradient. In this case, the sound waves propagating upstream are bent away from the wall, whereas those propagating downstream are directed toward the wall. This channeling of the sound energy into the pipe wall produces an additional attenuation of the downstream wave.

An analysis[12] for a two-dimensional linear shear wave shows the effect to be frequency dependent. For high frequencies ($\lambda << D$) the increase in the attenuation can be an order of magnitude.

In view of the two effects just described, it is obvious that even for low velocities (say 1 m/s in oil) and a transducer spacing of 1 m, an amplitude attenuation ratio of 5% is possible. Thus, it appears that this amplitude attenuation technique is a viable method of correlating fluid velocity even for the laminar-flow region.

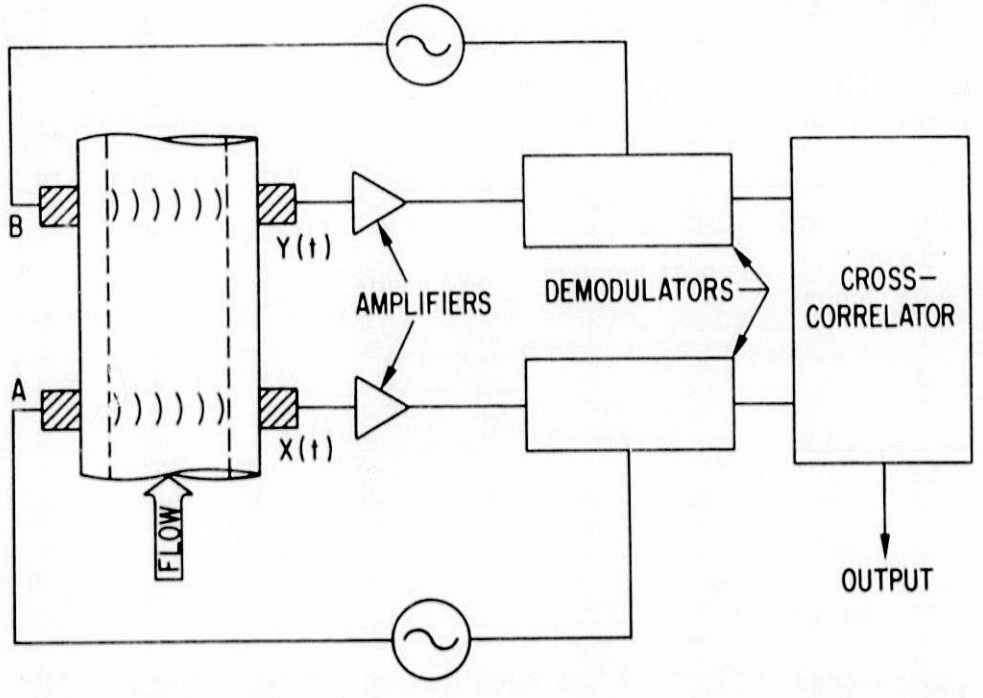

Fig. 4. Schematic Diagram of Acoustic Cross-correlation System for Low-velocity Fluid-flow Detection.

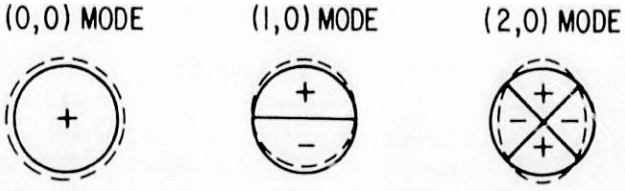

Fig. 5. Schematic Diagram of Various Mechanical Vibratory Modes Which Can Potentially be Used to Detect Low-velocity Fluid Flow.

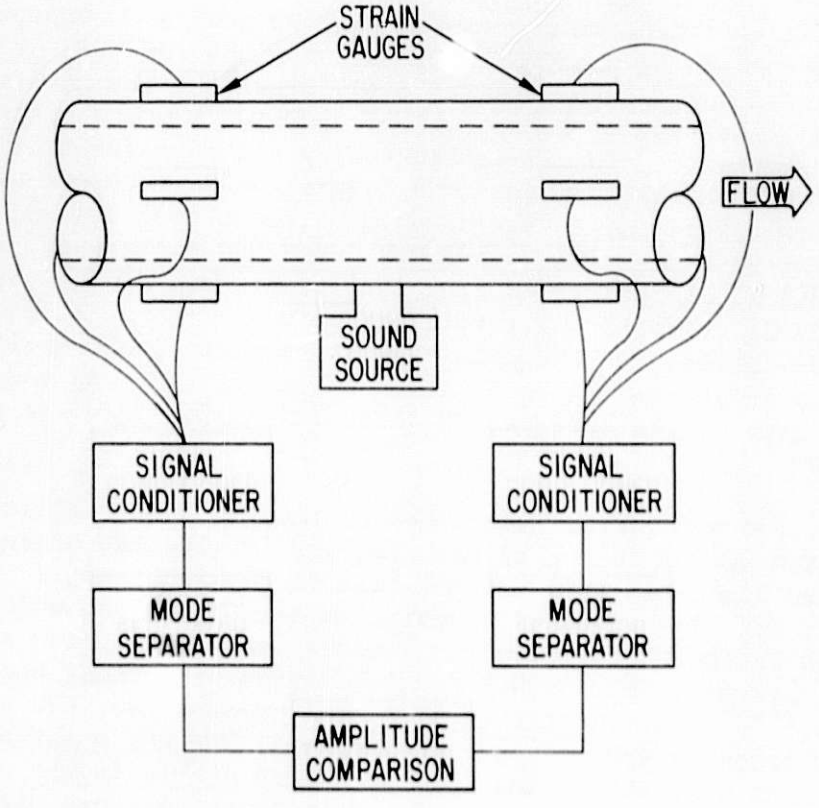

Fig. 6. Schematic Diagram of Strain-gauge System for Detection of Flexure Modes Caused by Fluid Flow, to be Used to Detect Low-velocity Fluid Flow.

Task C -- Corrosion Behavior of Materials in Coal-conversion Processes
(K. Natesan and T. C. Tiearney)*

The objectives of this program are to (1) develop uniaxial tensile data on four selected commercial alloys exposed to multicomponent gas environments, (2) experimentally evaluate the high-temperature corrosion behavior of iron- and nickel-base alloys in gas environments with a wide range of oxygen, sulfur, and carbon potentials, (3) evaluate deposit-induced hot-corrosion behavior of heat-exchanger and gas turbine materials with and without coatings after exposure to multicomponent gas environments, and (4) develop an approach that is based upon available thermodynamic and kinetic information for evaluating possible corrosion problems in various coal-conversion systems.

During this reporting period, the chemistry of the gaseous environments anticipated in different low-Btu gasifiers is examined and compared with those in high-Btu systems. The results from the analysis are used to evaluate the material interactions in low-Btu gaseous environments.

1. Background

In all gasification processes, the raw gas is a complex multicomponent mixture containing CO, CO_2, H_2O, CH_4, H_2, H_2S, and NH_3 or N_2. The composition will depend on the type of coal feedstock, the gasification agent (air or oxygen), the type of reactor (coal bed type), and the temperature and pressure of operation.[13] The available coal reserves range from low-sulfur, high-alkali, low-rank subbituminous and lignite coals (western U.S. coals) to high-sulfur, low-alkali, high-rank bituminous coals (eastern and midwest coals). The latter coals yield gases with high H_2S content and a large sulfidation potential, whereas gases from the former have a high potential for accelerated alkali corrosion of turbine materials. The heat content and caking tendency increase as the coal rank increases. These coal characteristics directly influence the composition of the raw gas and also dictate which reactor type can be used, which indirectly influences the gas composition.

All coal gasifiers, regardless of raw-gas heat content, are presently constructed with one of four coal-bed types.[14-15] The raw product gas from the widely used fixed-bed type has the highest heat content (in both air and oxygen modes), but also contains undesirable tars and pitch which precipitate out if the gas is cooled for desulfurization. In general, raw gas from this bed type contains more CH_4 and H_2S than that from other beds for the same input streams.[14-15] In contrast to fixed-bed product gas, the raw product gas from the fluidized-bed schemes contains no tars, but has a large particle loading at higher velocities, and more unreacted carbon in the ash.[14] Significantly lower H_2S contents are achieved in these reactors with the addition of limestone or dolomite to the bed. Entrained-bed gasifiers operate with extremely short residence times in the high-velocity reactant streams. The coal ash is removed as a molten slag due to the high temperature of the gas phase near the flame front. The resultant raw product gas contains very little, if any, CH_4 and has the lowest heating value of the three types discussed so far.[14-15] In the molten-bath (salt or iron) reactor, most of the sulfur

*Visiting Appointee from Exxon Research and Engineering Company.

is retained by the melt and the raw product gas is low in H_2S, CO_2, and H_2O.[16] When air is used instead of oxygen in any of these gasification schemes, a considerable fraction ($\sim$ 0.5) of the raw gas is nitrogen and the remaining gaseous species are present at reduced concentrations, approximately proportional to the degree of dilution.

The process conditions can also markedly affect the raw gas composition. As the system pressure increases, the volume fraction of CH_4 increases and that of CO decreases, while the H_2 fraction peaks at intermediate pressures. The heating value of the gas, which is predominantly determined by CH_4 content, also increases.[16] Temperatures vary widely in fixed- and entrained-bed processes from the bottom (combustion or flame zone) to the gas outlet at the top of the gasifier. Even the nearly isothermal fluidized-bed and molten-salt processes will have outlet temperatures somewhat below the bed (or bath) temperature. Temperature variations cause changes in gas composition throughout the gasifier vessel and influence material selection for metallic components that span large distances within the gasifier mainstream. As temperature increases in a given process, the volume fractions of CH_4 and CO_2 decrease, whereas the CO content increases and the H_2 content achieves a maximum value at temperatures between 1033 and 1144 K.

The process conditions which cause composition changes affect the variables, such as the partial pressures of oxygen and sulfur and the carbon activity, that are of interest in corrosion evaluation of materials exposed to coal-gasification environments. Considerable evaluation of high-temperature metallic corrosion in coal-gasification environments has been performed, particularly in the last five or ten years. The vast majority of the effort has focused on the high-Btu gasifier environments, the details of which are described elsewhere.[17-18] Recently, Natesan[19] has made a detailed state-of-the-art review of corrosion and mechanical behavior of materials for application in high-Btu gasification environments.

In contrast to the large effort on high-Btu environments, only in the last year have corrosion efforts in low-Btu atmospheres become appreciable. Preliminary results from programs at Sandia[17] and Lockheed[18] have shown that, for selected alloys, the MPC-chosen low-Btu gas composition proved to be more corrosive than the MPC-chosen high-Btu simulation gas. No doubt proprietary corrosion studies have been performed by commercial low-Btu gasifier manufacturers (Lurgi, McDowell-Wellman, etc.), but the information is not available to make a judicious selection of materials.

The purpose of the present research is to clarify the conditions present in many low-Btu gasifiers, so that the product-gas oxidant (O_2, S_2) potentials can be correlated with the corrosion behavior of candidate alloys. To this end, Incoloy 800 and Type 310 stainless steel, which are the major candidates for use in high-Btu gasification environments, were exposed in simulated low-Btu gasifier atmospheres, and the results have been used to compare the corrosiveness of the low- and high-Btu gasification environments.

2. Materials and Procedures

The Incoloy 800 and Type 310 stainless steel specimen materials were annealed sheet, 1.6 and 2.9 mm in thickness, respectively. The compositions of the alloys are listed in Table VI. Corrosion samples with

dimensions of 19 by 16 by 1.6-2.9 mm were polished through 240-grit SiC abrasive, rinsed with ethyl alcohol, and subsequently exposed to mixed-gas environments. The experiments were conducted in three-zone resistance-heated furnaces in which the temperature in the vicinity of the samples was controlled to within ∿ 1 K. The compositions of the gas mixtures were maintained by adjusting the relative flow rates of H_2-H_2S, CO-CO_2-CH_4, and H_2 entering the bottom of the reaction chamber. Table VII lists the gas compositions and the calculated[20] reaction potentials of the gas mixtures used in the experimental runs at 923 and 1144 K. Some gas mixtures (24-27) were selected to yield oxygen and sulfur potentials typical of low-Btu gasifiers (see Figs. 7 and 8). Additional mixtures with a wider range of composition were used to establish the sulfide-oxide transition boundaries of these alloys (18-23). Four gas mixtures (28-31), which simulate high-Btu process environments, were also used in experiments at 923 K for comparison with results from low-Btu gas mixtures. The experiments were, in general, of ∿ 110 hours duration.

Upon completion of the exposure experiments, polished sample cross sections were examined using a scanning-electron microscope equipped with an energy-dispersive x-ray analyzer to establish the type, thickness, morphology, and location of the corrosion products formed on the alloys. An electron microprobe was used to analyze for oxygen in the scales. Thermochemical diagrams were constructed for Type 310 stainless steel at both temperatures from the available thermodynamic data on reactions of iron, chromium, and nickel with oxygen and sulfur; the details are described in Ref. 19. Two short thermogravimetric tests were performed, one on each of the alloys at 1144 K in gas mixture 25. Weight-change data were normalized with respect to the initial surface area and plotted against time to compare the two alloys in this severe environment, which is representative of low-Btu gasification processes.

3. Results and Discussion

Information was excerpted from published literature on a number of commercial or pilot-stage gasifiers and analyzed with respect to the process characteristics described earlier. Tables VIII and IX summarize the results obtained for selected low- and high-Btu processes, respectively.[16,17,21-23] Several other processes (e.g., ATGAS, Hydrane, Koppers-Totzek, Slagging Lurgi, etc.) could be analyzed in a similar manner; however, the processes shown are sufficient to illustrate the four coal-bed types and the wide range of design pressures and temperatures that occur in coal-gasification processes. Wherever possible, the coal type (viz., the sulfur content) is listed to enable a better comparison of the processes. The gas compositions for the various processes are typical estimates only. The H_2S content in the gas from the MORGAS gasifier[17] was not specified, so a value of 0.5 vol % was chosen, which is typical of results from other fixed-bed gasifiers with high-sulfur coal. The numbers and symbols associated with the various gasifiers are those used in later figures. All of the high-Btu processes are pilot-stage second-generation units, whereas five of the low-Btu processes (1, 2, 3, 7, and 8) are commercially available first-generation units. The Metal Properties Council (MPC)-simulated high-Btu gasification atmosphere, with 0.5 vol % H_2S (from a range of 0.1 to 1.0 vol %),[17] is included with the high-Btu processes.

Since the total pressure in a coal-conversion process is relatively constant and the temperature varies considerably from a peak value in the gasifier region to a lower value in the primary cyclone regions of the system, the effect of temperature on the thermodynamic activity of the reactive elements (i.e., oxygen, sulfur, and carbon) at the design pressure of different processes is of interest. The gasifier characteristics in Tables VIII and IX were analyzed to establish oxygen, sulfur, and carbon potentials for the expected temperature range within each vessel. A generalized approach for the evaluation of reaction potentials in multicomponent gas mixtures has been presented elsewhere.[20,24] Figure 7 shows the dependence of the oxygen and sulfur partial pressures on temperature at the operating pressure for seven dry-ash low-Btu gasification processes. Figures 8 and 9 show similar information for the slagging (or molten-bath) low-Btu and high-Btu gasification schemes, respectively. The effect of oxygen- versus air-blown operation of a gasifier is shown in Fig. 7 for the Winkler (1' and 1) and Lurgi (2' and 2) processes.

Several important observations can be made from these figures. On an absolute basis, the oxygen partial pressure increases with temperature at a much higher rate than the sulfur partial pressure. However, if the partial pressures are normalized to the initial values of both species, the percent increase is approximately the same for both oxidants. Other observations can be drawn from a comparison of the ranges of the oxidant partial pressures of both gasification approaches. Because of the larger number of low-Btu gasifiers, the range of p_{O_2} is greater than for the high-Btu schemes in Fig. 9. However, at a given temperature, the oxygen partial pressure is generally higher in high-Btu processes than in low-Btu systems; this difference is more pronounced at lower temperatures. This observation is reinforced by the specific examples of the Winkler and Lurgi gasifiers mentioned previously. Both gasification processes have higher oxygen potentials when oxygen-blown (1', 2') than when air-blown. The difference is only slight for the Winkler process because it is a fluidized-bed gasifier with a relatively short residence time, which tends to minimize composition variations. Replacement of air with oxygen has a larger effect in the fixed-bed Lurgi gasifier. The sulfur partial pressure in both gasifiers is decreased by switching to oxygen-blown operation, but again the Lurgi process shows a greater reduction. Despite the larger number of processes and a much wider range of sulfur content in the coal reported in the list of low-Btu processes, the sulfur potential range is larger for the high-Btu gasifiers because the CO_2-Acceptor process, which uses dolomite as a sulfur sorbent in the fluidized bed to reduce the H_2S content in the raw gas, is included. Consequently, the sulfur potential curve for the CO_2-Acceptor process is nearly two orders of magnitude below the other high-Btu processes. Furthermore, with the use of high-sulfur coal, this process would produce a sulfur potential curve which approaches that of the next closest high-Btu process with low-sulfur coal.

In summary, the analysis shows that (1) the absolute change in oxygen pressure with temperature is greater than that for sulfur, (2) the range of oxygen and sulfur potentials is wider in low- and high-Btu processes, respectively, and (3) oxygen gasification produces a higher oxygen potential and a lower sulfur potential than air gasification. The last finding is particularly important because it suggests that low-Btu processes have, in general, more reducing atmospheres and higher sulfur potentials, a combination that can lead

to more severe material degradation via corrosion than is experienced in high-Btu atmospheres.

To experimentally verify this observation, two test temperatures were chosen in the present program, based on the following considerations: (1) The probable lower bound for gas temperatures in most of the gasifiers surveyed was ∿ 923 K, and (2) data are available on materials in corrosive gas mixtures at or near 1144 K. Published thermochemical diagrams for Incoloy 800 and Type 310 stainless steel at 1148 K are shown in Fig. 10.[25] The figure shows both the thermodynamic and the experimentally observed kinetic boundaries for the oxide to sulfide transition. The major difference between the two diagrams is the lower sulfur partial pressure of the Ni-Ni_3S_2 phase boundary for Incoloy 800 (32.5 wt % Ni) relative to that of Type 310 stainless steel (20 wt % Ni). There is little difference in the position of the kinetic boundary between sulfidation and oxidation in the 25-h tests (indicated by the dashed lines in Fig. 10) for the two materials. Apparently, the higher chromium concentration in Type 310 stainless steel (25 wt % Cr) offers no appreciable improvement in sulfidation resistance over Incoloy 800 (21 wt % Cr). A similar shift of the oxide/sulfide phase boundary to higher oxygen partial pressures has been reported by Perkins[17] in 48-h experiments performed in H_2S-H_2-H_2O gas mixtures.

The results from the present tests on Incoloy 800 and Type 310 stainless steel are summarized in Figs. 11-14. Because of the similarities between the thermochemical diagrams, results for both alloys are presented on diagrams for Type 310 stainless steel only. Figures 11 and 12 show the reaction potentials of the experimental gas mixtures, the experimental kinetic boundary, and the low- and high-Btu gasifier environments at 1144 K. The experimental gas mixtures lie in the phase regions corresponding to Cr_2O_3 or Cr_2O_3 plus FeS. In all cases, Cr_2O_3 formation is thermodynamically favored, but competing kinetic processes involving chromium, iron, oxygen, and sulfur determine which phase actually forms.

Figure 12 shows that the oxygen partial pressures in low-Btu gasifiers (open symbols) are generally lower than in high-Btu systems (solid symbols), whereas the sulfur partial pressures are higher in low-Btu processes. The Battelle-Union Carbide process is the only high-Btu process grouped with the low-Btu processes in terms of oxygen potential. If the H_2S content of the gas in the high-Btu processes was increased to values characteristic of high-sulfur coal feed, the sulfur potentials in the Synthane (1.1 vol % H_2S) and HYGAS (0.89 vol % H_2S)[26] processes would be nearly two orders of magnitude greater than those shown in Fig. 12. The sulfur potential in the CO_2-Acceptor process (0.09 vol % H_2S)[26] would only increase tenfold and the Bi-Gas process would experience no change at all, perhaps owing to the entrained-bed design.

The dashed curve in Fig. 12 represents the kinetic boundary determined from an analysis of the test results for both alloys. Gas mixtures that resulted in the formation of an external chromium sulfide or mixed chromium-iron sulfide scale are to the left of this boundary, and those which resulted in the formation of outer chromium-rich oxide scales, with or without internal sulfides, are to the right. This kinetic transition boundary is approximately three orders of magnitude higher in oxygen partial pressure than the thermodynamic boundary for Cr oxide/Cr sulfide. Only three of the low-Btu gasifier atmospheres would produce oxide scales after 110-h tests at 1144 K, and among those, Texaco and Winkler would also lead to a sulfidation mode of attack when

high-sulfur coal was used. Only the atmosphere in the Pullman-Kellogg molten-salt process is sufficiently low in H_2S to be within the oxide phase field of the diagram for high-sulfur Illinois #6 coal. The high-Btu process atmospheres are all within the oxide phase region for low-sulfur coal feedstocks, but high-sulfur coals would produce sulfidizing conditions in the Battelle-Union Carbide process, and cause the HYGAS and Synthane processes to exhibit borderline behavior.

Figures 13 and 14 show the experimental gas mixtures, kinetic boundary, and low- and high-Btu gasifier potentials at 923 K. Formation of nickel sulfide in these alloys becomes a factor with some of the experimental gas mixtures at this temperature, as evidenced in Fig. 13. The influence of exposure temperature on the corrosion behavior of Type 310 stainless steel can be evaluated from a comparison of data in Figs. 12 and 14. There are some similarities, most notably in the position of the low-Btu process potentials relative to the high-Btu process potentials with either low- or high-sulfur coal feedstock. However, the position of the kinetic boundary for the alloy is at significantly higher $p_{O_2}/p^{eq}_{O_2}$ values at the lower test temperature (Fig. 14); the absolute values are approximately five orders of magnitude higher than the thermodynamic equilibrium value at 923 K. Similar behavior is observed for Incoloy 800. This large difference can be attributed to the more sluggish kinetics at lower temperatures, which cause greater deviations from equilibrium conditions. Thus, there is a greater probability that gasifier product gases will be sulfidizing at the lower temperature. Only gas mixtures 30 and 31, which simulate the HYGAS, Synthane, and CO_2-Acceptor high-Btu gasifier conditions, produced oxide scales on Incoloy 800 and Type 310 stainless steel. Bi-Gas and Battelle-Union Carbide gasifier simulations exhibited borderline sulfidation behavior. The molten-salt and Texaco low-Btu processes exhibited relatively benign sulfidation conditions similar to the latter two high-Btu gasifiers. If high-sulfur coal were used in the high-Btu gasifiers, only the CO_2-Acceptor process would continue to form stable oxide scales.

SEM micrographs of scales formed on Incoloy 800 and Type 310 stainless steel specimens after exposure to gas mixtures 23, 24, and 25 at 1144 K are shown in Fig. 15. In gas mixture 25, which was the most corrosive, the alloys developed thick (Cr, Fe) sulfide scales with significant intergranular penetration of sulfur extending to the centerline of the specimens. Gas mixture 24, which establishes a lower p_{S_2} at the same p_{O_2} as mixture 25 (see Table VII), results in continuous Cr-rich oxide scales on the alloys. At still lower sulfur and oxygen potential, gas mixture 23 produces an external scale of Cr_3S_4 which is considerably thinner than the mixed sulfide formed in gas mixture 25.

Figure 16 further demonstrates the extreme corrosivity of gas mixture 25 at 1144 K, as evidenced by the thick, nonadherent sulfide layers formed on both alloys within short exposure times (7 and 25 h). The two sets of SEM micrographs are for samples exposed for 25 h in gas mixtures 41 and 49 (from Ref. 25), which are near the kinetic boundary defined by this study. Continuous oxide scales form under these conditions, which indicates that marked changes in scale morphology can result from only slight variations in oxygen and sulfur potential near the kinetic boundary. Figure 17 is a plot of weight change per unit surface area versus time for the two samples shown in the macrographs of Fig. 16. This diagram shows the marked similarities in the

parabolic growth rate of the scale on the two alloys and the large weight gains observed in the sulfidizing mode.

Examples of the scales formed on the alloys after exposure at 923 K are shown in Fig. 18. The sulfide scales are considerably thinner (up to 100 μm thick) than those formed at 1144 K (∿ 1.2 mm) upon exposure to gas mixtures 25 and 26. Among the mixtures used, gas mixture 25 provides the best approximation of the average low-Btu gasifier composition; however, both alloys form external scales of (Cr, Fe) sulfide upon exposure to this mixture. Gas mixture 29, which simulates the Bi-Gas gasifier, represents borderline oxidation-sulfidation behavior, as indicated by the patches of Cr_3S_4 and Cr_2O_3 scales shown at the surface. Lastly, gas mixture 30, which simulates both the HYGAS and Synthane processes, produces an external chromium-rich oxide scale which is thinner than any other oxide scale observed during this investigation (including scales produced by gas mixture 31, which simulates the CO_2-Acceptor process).

4. Conclusions

The corrosion potential of low-Btu gasifier atmospheres has been shown to be significantly more severe than that of high-Btu systems. This is primarily due to the lower oxygen potential caused by the dilution of the gas with N_2 from the air used in gasification. The simulated low-Btu environments produce sulfide scales on Type 310 stainless steel and Incoloy 800 which can approach 1.2 mm in thickness after 110 h at 1144 K, whereas the scale thicknesses at 923 K are considerably less ($\leq$ 100 μm). The phase boundary between Cr or (Cr, Fe) sulfide and Cr_2O_3 occurs at higher $p_{O_2}/p^{eq}_{O_2}$ values at the lower temperature. The $p_{O_2}/p^{eq}_{O_2}$ values are ∿ 10^3 at 1144 K and ∿ 10^5 at 923 K for these alloys. The differences in Ni, Fe, and Cr contents of Incoloy 800 and Type 310 stainless steel have virtually no effect on the position of the experimental sulfide-oxide phase boundaries. It was expected that longer exposure times would shift the kinetic (experimental) phase boundary to higher oxygen potential, but no consistent trend could be discerned from the results of this and two other studies for exposures between 25 and 110 h. Exposures of 1000 h or more were thought to be needed to establish this effect.[25]

A comparison of the environments in various high- and low-Btu processes shows that even the conventional high-chromium alloys such as Type 310 stainless steel and Incoloy 800 will develop a sulfide mode of attack in nearly all low-Btu atmospheres, regardless of the sulfur content of the coal feedstock. The Pullman-Kellogg molten-salt process was found to be least corrosive, but even this process environment would favor sulfide scale formation on the conventional alloys at lower temperatures.

It is inevitable that materials availability, selection, and reliability will play a major role in the utilization of coal via low-Btu gasification schemes. Greater emphasis must be placed on novel design approaches and alternate materials to make these schemes viable. Clearly, the gaseous corrosion of Incoloy 800 and Type 310 stainless steel is unacceptably severe in environments that simulate low-Btu gasification processes. However, duplex alloys or coatings with different bases (i.e., Fe-Cr-Al, Ni-Cr, Co-Cr, etc.) should be investigated in greater detail for application in these systems. Several of these alternative alloy systems are being examined at ANL in a

continuation of the work reported here. Furthermore, other potentially degrading effects that have not been addressed here, such as erosion, deposit corrosion, and thermal cycling, are certain to have an influence on material performance. The deposit-corrosion aspect of gasifiers is also being examined as part of the ongoing work on advanced-alloy corrosion in low-Btu gasifier atmospheres.

TABLE VI. Alloy Compositions in Weight Percent

	C	Mn	Si	Cr	Ni	Al	Ti	Fe
Incoloy 800	0.05	0.8	0.5	21.0	32.5	0.4	0.4	Bal.
Type 310 SS	0.25	2.0	1.5	25.0	20.0	-	-	Bal.

TABLE VII. Reaction Potentials Established in Experimental Runs

Gas Identification Number	Gas Composition (vol %)					Reaction Potentials[a]		
	CO	CO_2	CH_4	H_2	H_2S	P_{O_2}, atm	P_{S_2}, atm	a_C
18	31.8	36.4	22.7	8.7	0.36	8.2×10^{-24} 1.9×10^{-19}	7.0×10^{-10} 3.9×10^{-8}	0.848 0.255
19	0.67	0.77	0.48	97.9	0.15	2.65×10^{-26} 5.2×10^{-22}	2.3×10^{-11} 2.0×10^{-9}	0.090 0.137
20	4.65	5.31	3.32	86.7	0.06	8.1×10^{-25} 8.4×10^{-21}	6.0×10^{-12} 3.3×10^{-10}	0.650 0.252
21	4.65	5.31	3.32	86.4	0.30	8.1×10^{-25} 8.5×10^{-21}	1.5×10^{-10} 8.5×10^{-9}	0.653 0.251
22	27.94	31.93	19.96	20.09	0.08	7.2×10^{-24} 1.5×10^{-19}	3.5×10^{-11} 1.9×10^{-9}	0.865 0.261
23	4.64	5.30	3.31	86.6	0.13	8.1×10^{-25} 8.4×10^{-21}	3.0×10^{-11} 1.7×10^{-9}	0.649 0.251
24	22.86	45.70	7.62	23.40	0.42	1.2×10^{-23} 4.2×10^{-18}	4.6×10^{-10} 4.1×10^{-8}	0.992 0.043
25	22.5	45.0	7.5	24.06	0.94	1.2×10^{-23} 4.1×10^{-18}	1.1×10^{-8} 9.4×10^{-7}	0.993 0.043
26	6.0	12.0	2.0	77.37	2.63	2.4×10^{-24} 1.8×10^{-19}	1.8×10^{-8} 1.0×10^{-6}	0.800 0.079
27	12.5	25.0	4.17	57.47	0.86	5.6×10^{-24} 9.2×10^{-19}	3.2×10^{-9} 2.0×10^{-7}	1.000 0.064
28	-	51.28	-	48.44	0.28	3.3×10^{-23}	9.2×10^{-10}	0.412
29	-	88.89	-	11.01	0.10	1.0×10^{-21}	1.7×10^{-8}	0.034
30	-	83.33	-	16.62	0.05	4.2×10^{-22}	1.0×10^{-9}	0.071
31	-	64.52	-	35.46	0.02	7.4×10^{-23}	1.9×10^{-11}	0.261

[a]Upper and lower values are for 923 K and 1144 K tests, respectively. Gas mixtures 28-31 were only tested at 923 K.

TABLE VIII. LOW-BTU GASIFIER DESCRIPTIONS

GASIFIER	SYMBOL	BED TYPE	PRESSURE (ATM)	WT % S IN COAL	MAX. TEMP (°C)	ROOM TEMPERATURE GAS COMPOSITION (VOL. %)						
						CO	CO_2	H_2	CH_4	H_2O	H_2S	N_2
Winkler	1 ⊗	Fluidized	1.0	≤1	980	19.0	6.2	11.7	0.5	11.5	0.13	51.1
Lurgi	2 □	Fixed	30.6	NA[a]	760	13.3	13.3	19.6	5.5	10.1	0.6	37.6
U-GAS	3 △	Fluidized	23.8	NA	1040	17.0	8.8	11.6	4.1	12.0	0.6	45.4
Westinghouse	4 ⊠	Fluidized	16.3	NA	980	19.5	8.8	11.4	0.1	11.2	0.4	48.6
GEGAS[b]	5 ○	Fixed	6.0	IL. #6 (3-4)	1200	25.8	7.3	13.5	3.7	-	0.95	48.6
MORGAS[b]	6 ◇	Fixed	2.0	IL. #6 (3-4)	1010	18.9	10.1	14.1	2.0	-	0.5	51.3
Woodall-Duckham	7 ☆	Fixed (2 Stage)	1.0	NA	1200	28.2	4.5	17.0	2.7	-	0.5	47.1
Wellman-Galusha	8 ●	Fixed	1.0	NA	1315	24.9	6.2	18.7	0.6	-	0.3	49.3
Combustion Engr.	9 ▽	Entrained	1.0	Pittsburgh #8 (>2)	1650	21.8	3.8	9.6	-	5.9	0.32	53.7
Texaco	10 ⬠	Entrained	88.0	0.46	1650	23.5	3.1	13.0	0.02	-	0.14	60.3
Pullman-Kellogg	11 ⬡	Molten Na_2CO_3	28.0	IL. #6 (3-4)	980	28.3	3.1	13.8	1.5	2.35	0.1	50.85

[a] Not available.
[b] Contains small amounts of O_2 also.

TABLE IX. HIGH-BTU GASIFIER CHARACTERISTICS (USING WESTERN COAL WITH $\leq$1% S)

GASIFIER	SYMBOL	BED TYPE	PRESSURE (ATM)	TEMP. (^{o}C)	ROOM TEMPERATURE GAS COMPOSITION (VOL. %)						
					CO	CO_2	H_2	CH_4	H_2O	H_2S	NH_3
B-UC	■	Fluidized	7	980	26	5	49	6	14	0.3 [NA]	1
CO_2 Acceptor	★		20	870	11	6	52	3	28	0.03 [0.09]	
HYGAS	▲		80	950	21	21	17	15	25	0.1 [1.1]	
Synthane	◆		70	980	9	21	19	12	36	0.1 [0.89]	
Bi-Gas	▼	Entrained	70	930-1650	12	13	15	7	52	0.5 [0.5]	
MPC Simulation	●	-	1	650-870	18	12	24	5	39	0-1 (0.5 used)	

[a] [ ] = H_2S value for eastern high-sulfur coal.

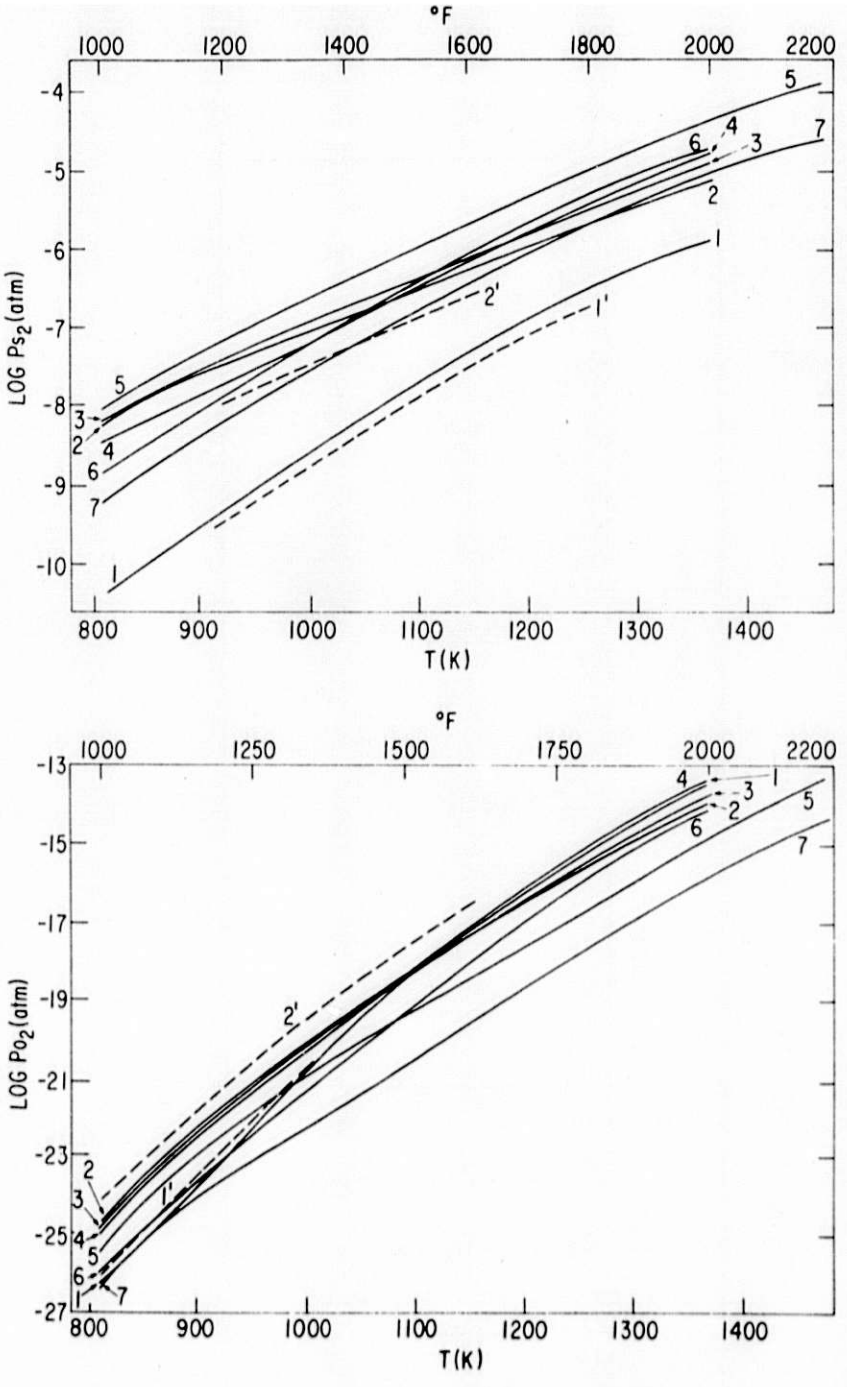

Fig. 7. Sulfur and Oxygen Partial Pressures as Functions of Temperature for Dry-ash Low-Btu Gasifiers 1-7, and Intermediate-Btu Gasifiers 1' and 2'.

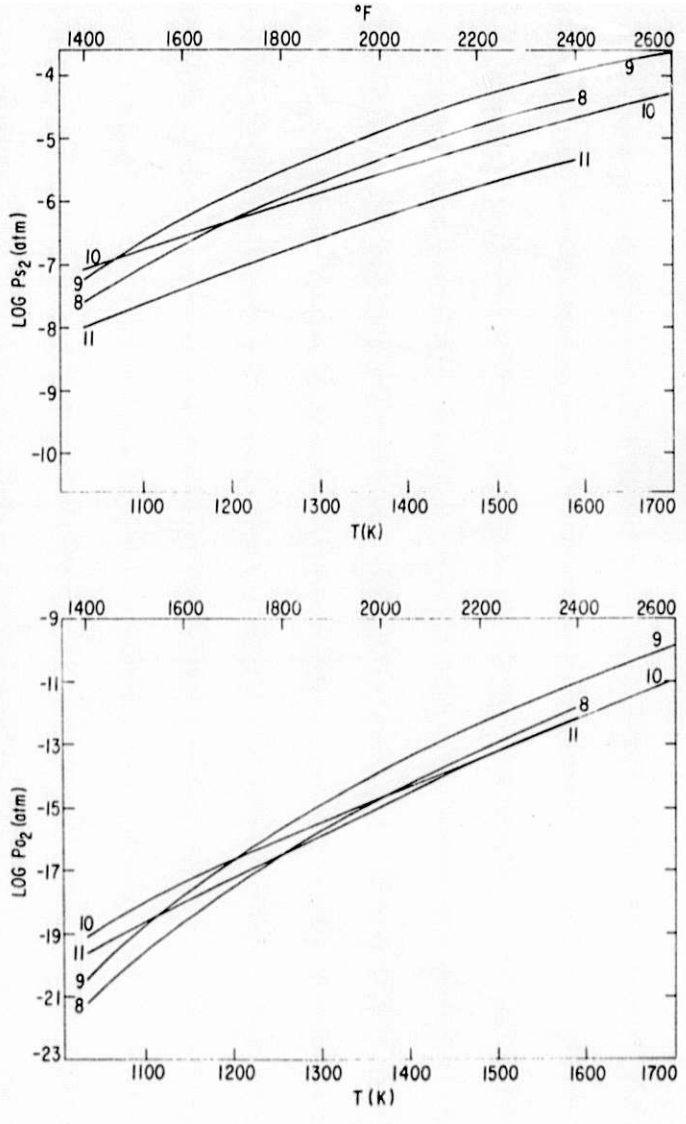

Fig. 8. Sulfur and Oxygen Partial Pressures as Functions of Temperature for Slagging and Molten-bath Low-Btu Gasifiers 8-11.

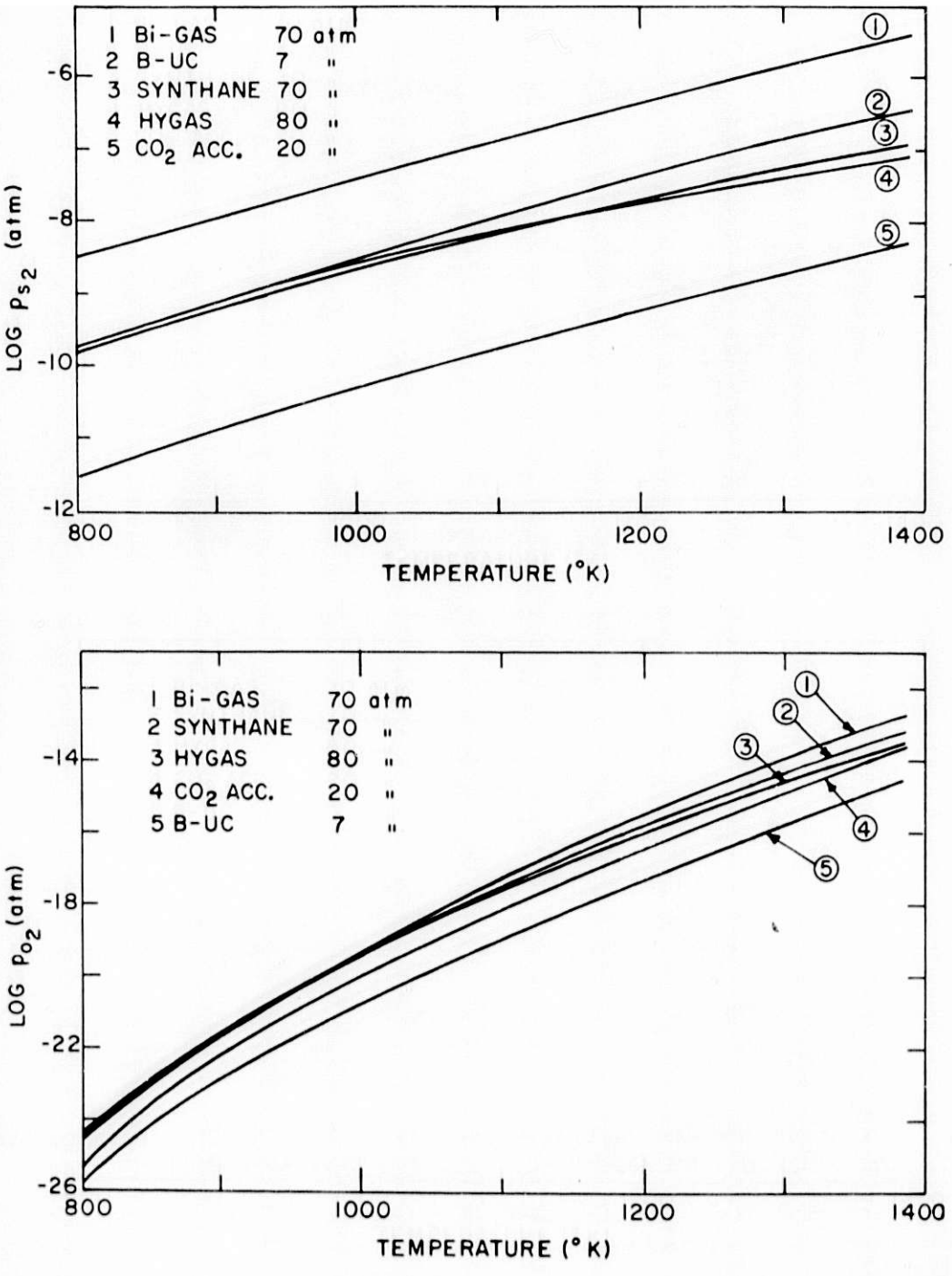

Fig. 9. Sulfur and Oxygen Partial Pressures as Functions of Temperature for the Five High-Btu Pilot Plant Gasifiers.

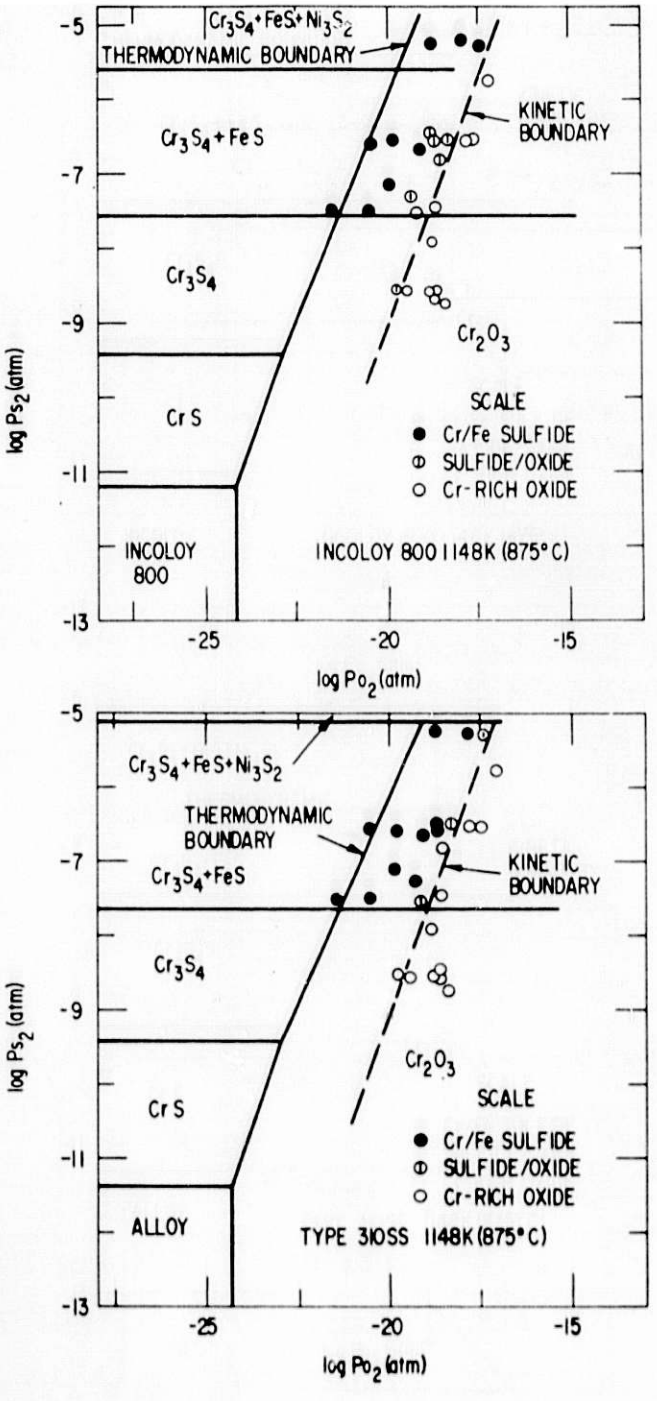

Fig. 10. Thermochemical Phase Diagrams for Incoloy 800 and Type 310 Stainless Steel at 1148 K, Showing the Types of Scale Formed as a Function of Oxygen and Sulfur Partial Pressures in the Gas Environment. Data from Ref. 13.

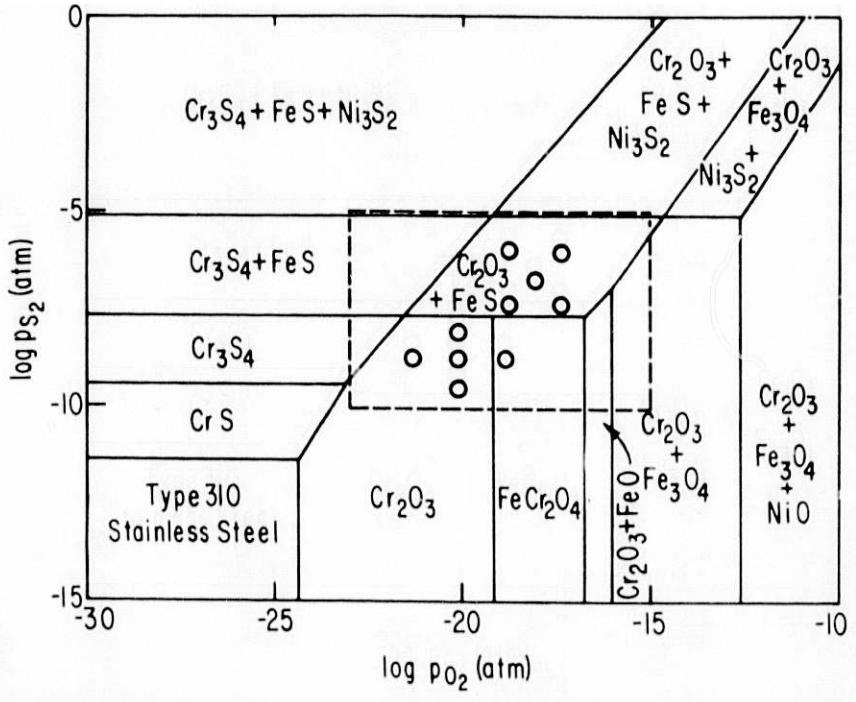

Fig. 11. Calculated Thermochemical Diagram for Type 310 Stainless Steel at 1144 K, Showing the Experimental Gas Potentials.

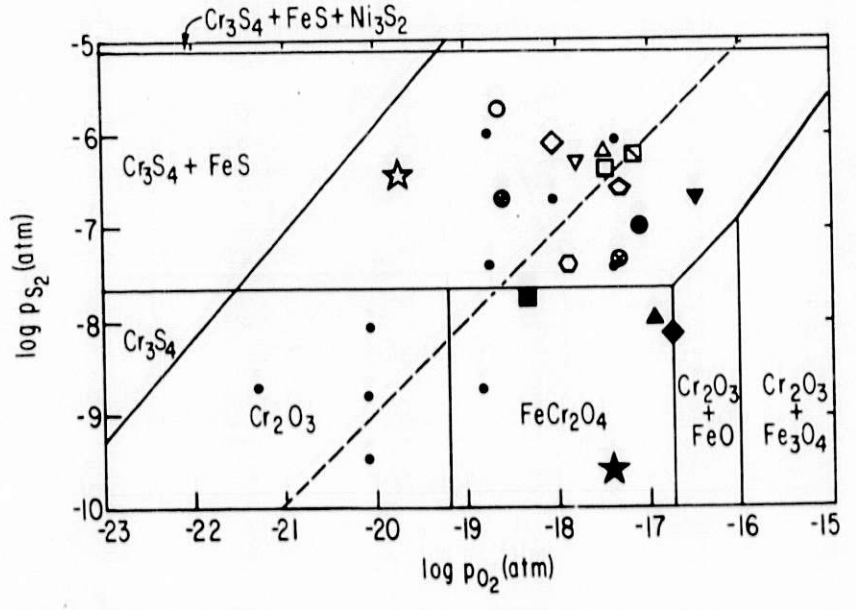

Fig. 12. Magnification of Fig. 11, Showing the Experimental Kinetic Boundary and the Low- and High-Btu Gasifier Conditions at 1144 K.

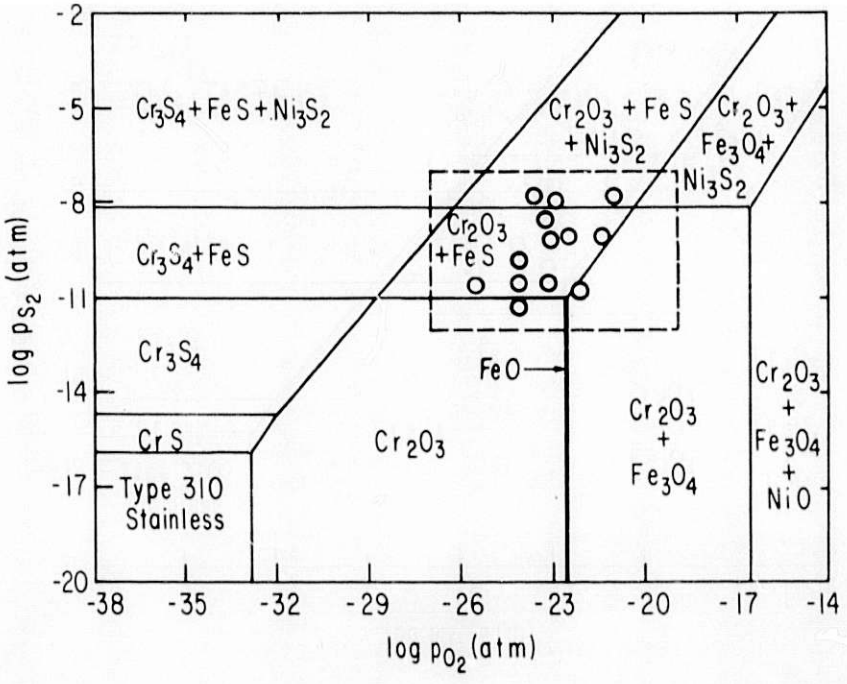

Fig. 13. Calculated Thermochemical Diagram for Type 310 Stainless Steel at 923 K, Showing the Experimental Gas Potentials.

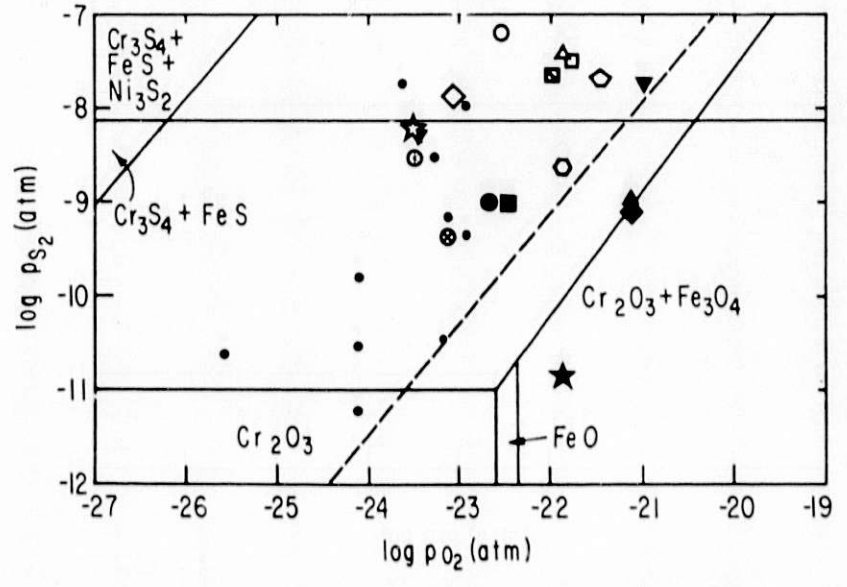

Fig. 14. Magnification of Fig. 13, Showing the Experimental Kinetic Boundary and the Low- and High-Btu Gasifier Conditions at 923 K.

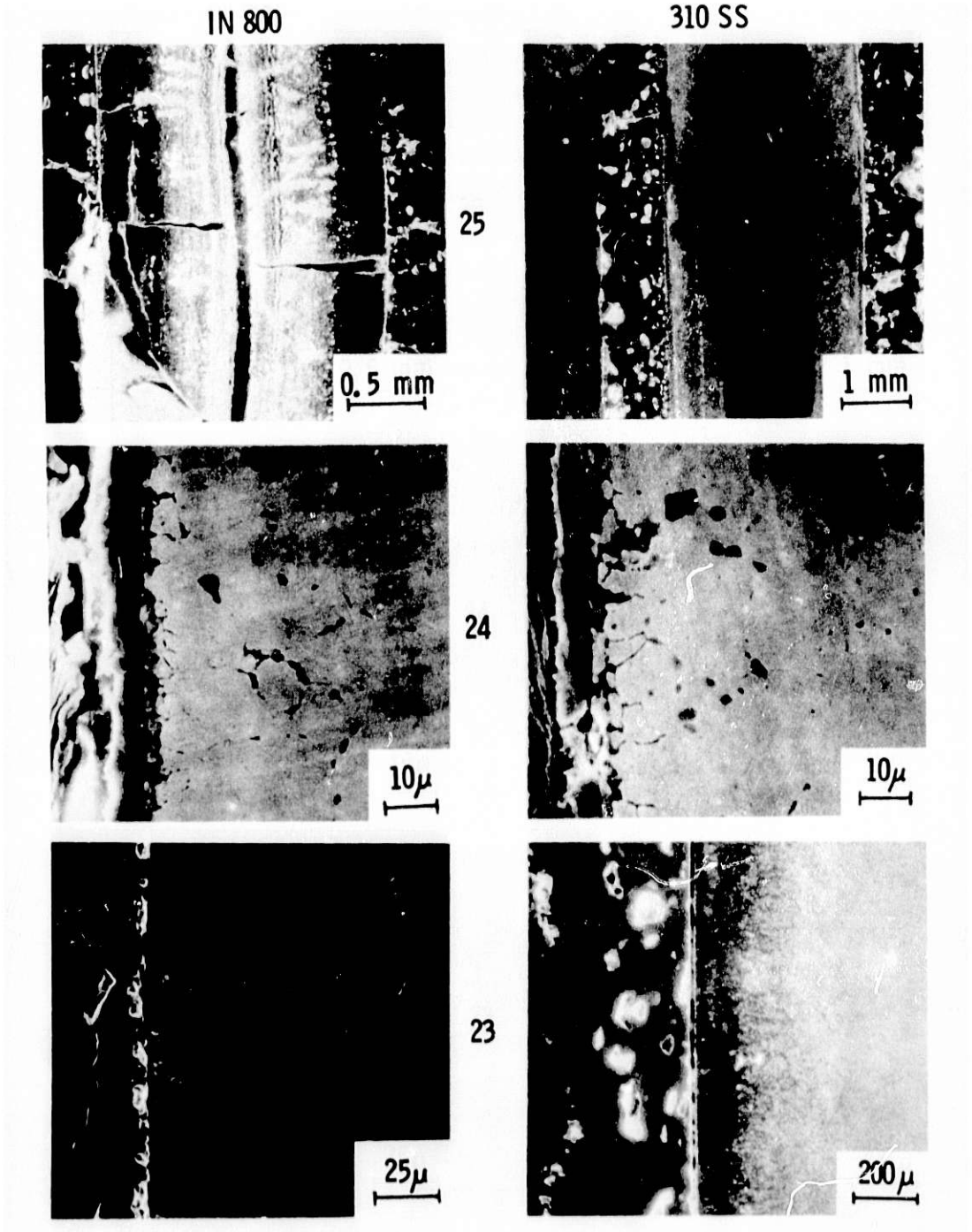

Fig. 15. SEM Photographs of Incoloy 800 and Type 310 Stainless Steel Exposed for 110 h at 1144 K in Gas Mixtures 25, 24, and 23.

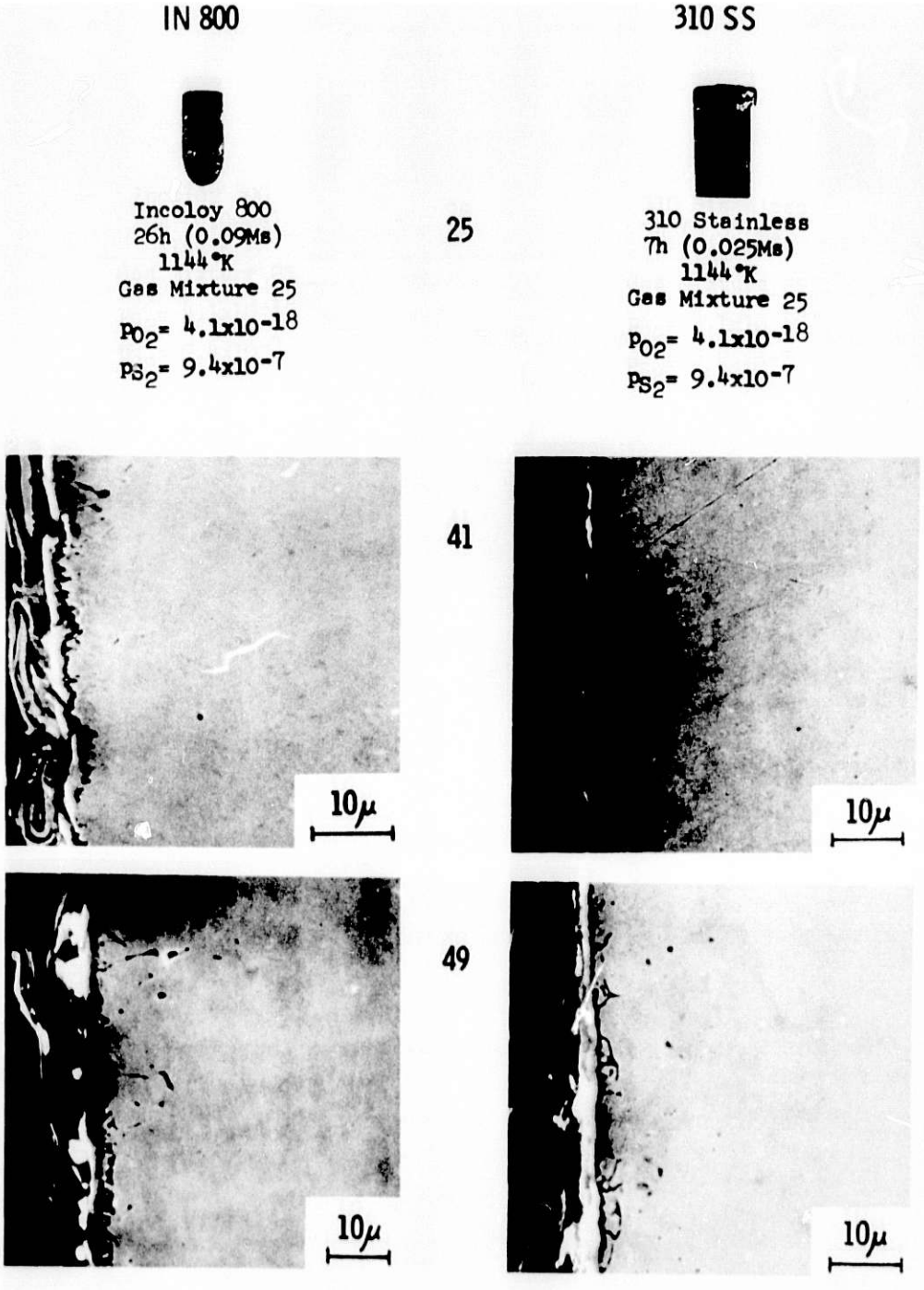

Fig. 16. TGA Samples Exposed to Gas Mixture 25 and Corrosion Specimens Exposed to Gas Mixtures 41 and 49, all at 1144 K. The exposure of 310 SS to mixture 25 was for 7 h; all other exposures were for 25 h.

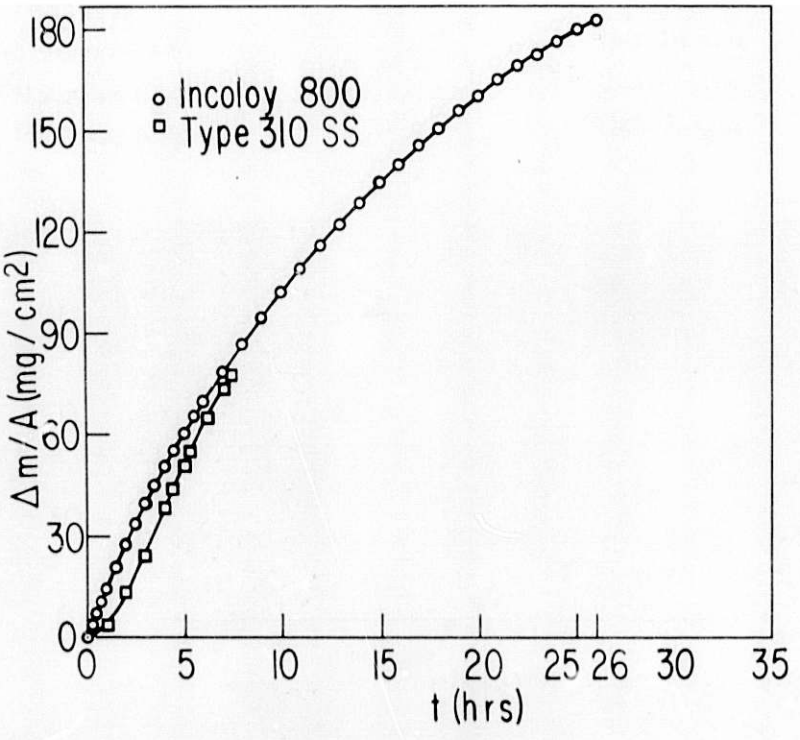

Fig. 17. Weight Gain per Unit Surface Area as a Function of Exposure Time for Incoloy 800 and Type 310 Stainless Steel in Gas Mixture 25 at 1144 K.

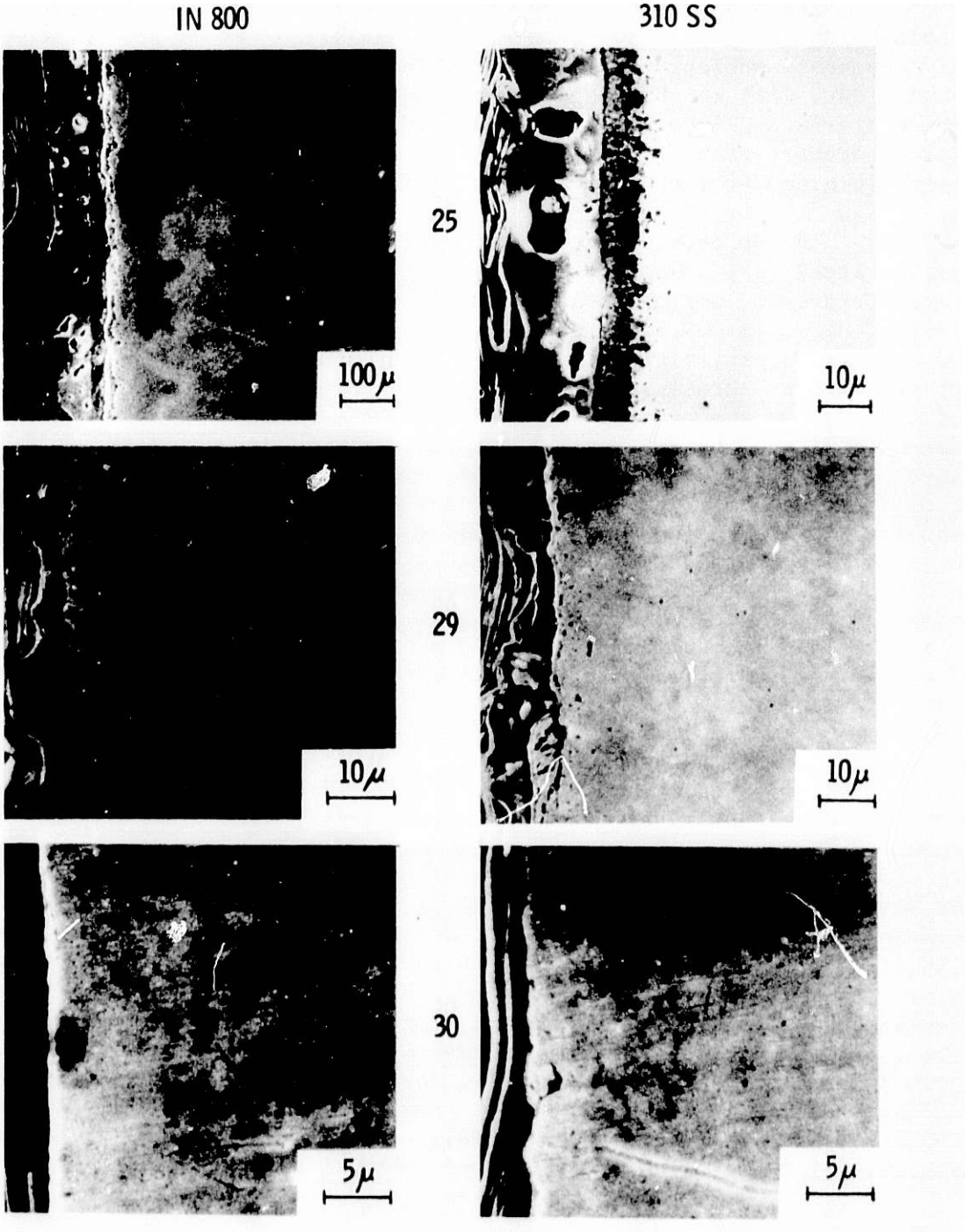

Fig. 18. SEM Photographs of Incoloy 800 and Type 310 Stainless Steel Exposed for 110 h at 923 K in Gas Mixtures 25, 29, and 30.

Task D -- Erosion Behavior of Materials in Coal-conversion Processes
(J.Y. Park and W.J. Shack)

The objectives of the erosion program at ANL are to develop an engineering data base and the necessary analytical tools for rational design of components subject to erosive wear in coal-conversion plants. Engineering design data will be obtained from erosion tests which will be performed at temperatures and in atmospheres designed to simulate actual plant conditions. The laboratory results will be compared with in-situ measurements currently being obtained from the NDT program at ANL.

In the previous quarters, corrosion calibration tests on 1015 carbon steel (CS), Type 304 stainless steel (SS), Incoloy 800, and Stellite 6B were performed. Corrosion calibration tests in a simulated gasifier atmosphere (18 CO, 12 CO_2, 5 CH_4, 24 H_2, 39 H_2O, 1 NH_3, 1 H_2S in vol. %) at 816°C were reported previously.[27,2] Significant amounts of corrosion were observed in all alloys. Cross sections of the specimens were examined by optical metallography, and material degradation due to corrosion was measured in terms of weight change, loss of substrate thickness, scale formation, and internal corrosion. Room-temperature erosion calibration tests were performed on 1015 CS, Type 304 SS, Incoloy 800, RA310 SS, and Stellite 6B specimens using the new specimen holder and 100-grit (150-μm) alumina particles at an impingement velocity of 22 m/s and angles ranging from 6 to 36°. Erosion rate (mass loss/mass impacted) was calculated from weight loss. The rate is in the range of 0.03-0.09 mg/g, which is about 7 times lower than that obtained in earlier tests at 70 m/s using 240-grit (50-μm) alumina.[28] However, the variation is consistent with the expected dependence of erosion rate on velocity.

During the present quarter, an additional room-temperature erosion calibration was performed. The results of the test are in good agreement with those of the previous test. Erosion rates (mass loss/mass impacted) are shown in Table X. A 24-h erosion-corrosion test on 1015 CS, Type 304 SS, Incoloy 800 and Stellite 6B was performed in a simulated gasifier atmosphere at 816°C, using 100-grit (150-μm) alumina at an impingement velocity of 22 m/s and angles ranging from 16 to 81°. Erosion-corrosion rate (mass loss/mass impacted) was calculated from weight loss (Table XI). Erosion-corrosion rate, however, should not be taken as a direct representation of material degradation rate, because the total weight loss, which was used to calculate the erosion-corrosion rate, includes weight loss due to erosion and weight gain due to corrosion. For example, the erosion-corrosion rate of 1015 carbon steel in Table XI is smaller than that of other materials, but the amount of material degradation of 1015 carbon steel is largest. Detailed analysis of the erosion-corrosion test results will follow.

TABLE X. Erosion Calibration Test[a] Results (II)

Material	Impingement Angle			
	16°	26°	36°	81°
1015 Carbon Steel	0.05[b]	0.05	0.03	0.02
Type 304 Stainless Steel	0.05	0.04	0.04	0.02
Incoloy 800	0.06	0.05	0.04	0.03
RA310 Stainless Steel	0.06	0.05	0.04	0.03
Stellite 6B	0.06	0.04	0.04	0.03

[a]In air, at room temperature.

[b]Erosion rates in mg/g.

TABLE XI. Erosion-corrosion Test[a] Results

Material	Impingement Angle			
	16°	26°	36°	81°
1015 Carbon Steel	0.03[b]	0.01	0.01	0.00
Type 304 Stainless Steel	0.09	0.06	0.06	0.06
Incoloy 800	0.07	0.07	0.07	0.09
RA310 Stainless Steel	0.06	0.07	0.07	0.10
Stellite 6B	0.08	0.07	0.06	0.08

[a]24 h in simulated gasifier environment at 816°C, with 150-μm alumina at 22 m/s.

[b]Erosion rates in mg/g.

Task E -- Failure Analysis *(D.R. Diercks, J.Y.N. Wang, and G.M. Dragel)*

1. Experimental Thermowells for IGT Ash Agglomerating Gasifier

Seven experimental thermowells have been prepared for trial exposure in the IGT Ash Agglomerating Gasifier (U-Gas) Pilot Plant, as described in the previous report.[1] At present, experimental thermowells 2, 3, and 7 are installed at positions approximately 1.1, 1.4, and 2.3 m (3.5, 4.5, and 7.5 ft), respectively, above the normal operating height of the bed. Thermowell 1, which is an uncoated Haynes 188 thermowell identical to thermowell 2, is installed at a somewhat more erosive location approximately 0.4 m (1.4 ft) above the top of the bed.

Four pilot-plant runs, each approximately five days long, have been completed with the first four experimental thermowells in place. The first three of these runs were made using relatively high-sulfur Pittsburgh-seam coal, and the fourth run was made using a mixture of Kentucky nos. 9 and 11 coals. The bed operating temperature for all four runs was typically in the range from 1024 to 1066°C (1875 to 1950°F). None of the four thermowells has exhibited significant degradation to date, and an undetermined number of additional runs are planned before the thermowells are removed for examination.

2. Solids Transfer Line from IGT HYGAS Pilot Plant

An analysis of failed internal transfer line components from the IGT HYGAS Pilot Plant referred to in the previous progress report[1] has been completed. The failed line was made of 7.6-cm (3-in.)-ID Schedule 80 pipe welded together at several points along its length using 7.6-cm (3-in.)-long, 9.5-cm (3.75-in.)-ID Schedule 120 sleeve couplings. Chemical analyses revealed that both RA 330 and Incoloy 800 were used to fabricate the piping and couplings. The weld filler metal was the high-nickel alloy Inconel 182. Failure occurred by severe localized corrosive attack of the weld metal at the OD, and the previous report tentatively attributed this attack to sulfidation and the probable formation of the low-melting-point Ni-Ni_3S_2 eutectic.

Results obtained since that previous progress report was published have tended to support the sulfidation hypothesis.[29] SEM and x-ray microprobe analyses of the corrosion product and underlying weld and base metal confirm the presence of high-sulfur regions in the surface scale and indicate that high nickel concentrations are often found in the same regions. A thermochemical analysis of phase stabilities in the HYGAS environment at 871°C (1600°F) has also been performed for both a Fe-20Cr-35Ni base metal (corresponding approximately to RA 330 and Incoloy 800) and for the Inconel 182 weld metal. The corresponding thermochemical diagrams are shown as Figs. 19 and 20. It may be seen from these diagrams that the chromium oxide and iron oxide phases are predicted to be stable in the base metal at this temperature. Assuming that chemical equilibrium between the environment and the base metal is actually attained, no significant corrosive sulfide attack of the base metal would be expected. For the Inconel 182 weld metal, however, the phase field boundaries are shifted somewhat by the higher nickel content (~ 67 wt. %) of this alloy. Nickel sulfide (in this case Ni_3S_2) has replaced iron oxide as the stable phase along with Cr_2O_3, and severe corrosive attack of the weld metal would be expected. Kinetic effects and local departures

from equilibrium will, of course, influence the phase stabilities actually observed. Nonetheless, this thermochemical analysis supports previous microstructural evidence that the transfer line failed owing to sulfidation attack of the high-nickel weld filler metal.

3. Thermocouple from IGT HYGAS Pilot Plant

The previous report[1] described preliminary results from the investigation of a failed thermocouple from the IGT HYGAS coal gasification pilot plant. The failed thermocouple was a Type K (Chromel/Alumel) device with a Type 310 stainless steel sheath and MgO insulation. The sheath ruptured after approximately 361 hours of service in the steam-oxygen gasifier zone of the HYGAS reactor at temperatures ranging from 871 to 982°C (1600 to 1800°F) and pressures of from 3.5 to 4.5 MPa (500 to 650 psi). The thermocouple was not protected by a thermowell. X-ray diffraction results described in the previous report indicated that the MgO insulation had been converted to $Mg(OH)_2$ in the failed regions, and the accompanying volume expansion apparently contributed to the splitting of the sheath.

Since that time, further work has been carried out in an attempt to determine what caused the initial penetration of the thermocouple sheath, thereby permitting the water vapor present in the coal-gas environment to react with the MgO insulation. Electron microprobe and metallographic examinations indicate that no significant corrosive attack is present at the OD surface of the sheath, and the surface layer present here is primarily Cr_2O_3. At the ID surface, however, significant chromium sulfide formation is observed, particularly at grain boundaries. Figure 21 shows SEM and microprobe images obtained from a region near the ID surface, and shows the concentration of Cr, S, and O at the grain boundaries. Several cracks and porous regions, apparently preexisting, were also found in the sheath wall by metallography. It appears that these preexisting flaws were the underlying cause of the present failure. The access of the gasifier environment to the ID of the thermocouple through these flaws permitted the water vapor present in this environment to react with the MgO insulation inside the sheath. In addition, limited supplies of sulfur and oxygen were admitted, and these elements reacted with the ID surface of the sheath. Since the rate for sulfide formation is significantly greater than that for oxide formation, the sulfides seen in Fig. 21 were probably formed before a sufficiently thick and continuous oxide layer could be formed at the ID surface to provide protection. Final sheath rupture apparently resulted from a combination of the excessive stresses imposed by the formation of $Mg(OH)_2$ inside the sheath and the embrittlement of the ID region due to sulfur attack. Preparation of a final report on this failure is in progress.

4. Review of Failure Analyses

A review of the more important failure analyses performed at Argonne on components from coal-gasification pilot plants over the past six years has recently been performed.[30] Table XII summarizes the results of this review for 46 analyses performed during that time period. Almost all of the more significant analyses are included in the table, but the results of brief and informal examinations performed under circumstances where a complete documentation of operating conditions or other essential information

was unavailable have been deleted. The analyses are listed according to pilot plant, and failures are grouped by type rather than chronologically. The fact that more analyses are listed for some pilot plants than for others does not necessarily indicate differences in overall reliability, but rather reflects the extent to which the various plants participated in the ANL failure analysis program. Failure analyses that were performed at the pilot-plant facility or at other laboratories are not included here. The summaries given in the table are necessarily brief because of space limitations; the reader interested in the details of a particular analysis should consult the sources cited in Ref. 30.

TABLE XII. Summary of Selected Failure Analyses Performed at Argonne National Laboratory on Coal-gasification Pilot Plant Components

Component	Operating Environment	Material	Description of Failure	Recommendations
IGT HYGAS Pilot Plant				
1. Thermocouple in pretreatment vessel (1st failure)	Crushed-coal fluidized bed and oxidizing gas at max. design temp. of 427 C	Type 316 SS thermowell; Fe-constantan thermocouple	Severe oxidation of thermowell and melting of constantan wire at junction due to overtemperature	Maintain better temperature control
2. Thermocouple in pretreatment vessel (2nd failure)	See above	Type 310 SS thermowell; Fe-constantan thermocouple	Grain-boundary sulfidation and melting of thermowell due to overtemperature	Maintain better temperature control; avoid clinker buildup
3. Pretreatment vessel cooling bundle (1st failure)	See above	SA106, Grade 2 carbon steel	Tube buckling and rupture due to overtemperature	Maintain better temperature control
4. Pretreatment vessel cooling bundle (2nd failure)	See above	SA106, Grade 2 carbon steel	Severe corrosive attack and tube rupture due to overtemperature	Maintain better temperature control
5. Gasifier startup burner expansion bellows	H_2 at OD, N_2 at ID; max. design temp. of 90 C	Type 321 SS	Oxidation and local melting due to overtemperature (burner backfire?)	Maintain proper burner combustion conditions
6. Thermocouple sheath in SOG gasifier	Coal-char fluidized bed and oxidizing gas at max design temp of 1090 C	Inconel 702	Severe embrittlement and cracking due to internal oxidation	Replace with Type 310 SS
7. Gasifier internal solids transfer line	Oxidizing and sulfidizing product gas at 540 to 980 C	Incoloy 800, RA 330, and Inconel 182	Severe corrosive attack at welds due to sulfidation of high-nickel Inconel 182 weld metal	Use lower-nickel weld filler metal

TABLE XII (continued)

Component	Operating Environment	Material	Description of Failure	Recommendations
8. Hinge pin from solids transfer valve	Coal-char fluidized bed and oxidizing gas at max design temp. of 1090 C	RA 330	Deformation and galling due to overload	Reduce loading; use alloy with better high-temperature strength
9. Gasifier transfer line expansion bellows	N_2 at OD, product gas and char at ID; max. temp. 650 C	Incoloy 800	Pitting perforations from ID due to chlorides from coal char deposits	Eliminate deposits; replace with alloy more resistant to pitting
10. Nitrogen purge line from SOG	Oxidizing gas environment at 760 to 870 C	Type 316 SS	Grain-boundary embrittlement and fracture due to sulfidation from ID	Eliminate sulfur (origin uncertain)
11. Instrument lines in steam-oxygen injection system	Superheated steam plus occasional O_2 at 316 C; intermittent operation	Types 304 and 316 SS	Inter- and transgranular SCC due to O_2 and residual chlorides in steam plus residual stresses at bends	Replace with Incoloy 800; avoid cold bending
12. Water purge line	City water at 150 C; externally insulated and exposed to weather	Type 316 SS; asbestos insulation	Transgranular SCC from OD due to chlorides leached from insulation and residual stresses due to cold forming	Use lower chloride insulation; reduce cold forming
13. High-pressure water line	See above	See above	Transgranular SCC from ID due to chlorides in city water and residual stresses due to cold forming	Use deionized water; reduce cold forming
14. Water sight-glass purge lines	City water at 93 C	Type 304 SS	See above	See above
15. Welded tee fitting on spent char carrier line	Steam at 290 C with occasional surges at 870 C followed by quench at 90 C	Type 316 SS	Cracking at ID due to thermal shock	Avoid or reduce abrupt temperature changes
16. Leaf springs from H_2 gas compressor	H_2 plus some CO, CO_2, and H_2O at 24 to 105 C	Type 416 SS	Fracture at surface pits due to improper heat treatment (cause of pitting uncertain)	Use correct heat treatment; avoid H_2O condensation

TABLE XII (continued)

Component	Operating Environment	Material	Description of Failure	Recommendations
17. Pipe from quench separator enclosure	Toluene and H_2O solution at 205 C	Incoloy 800	IGSCC near welds due to sensitization, residual welding stresses, and chlorides in water-toluene solution	Control chlorides, stress relieve welds, possibly replace with Incoloy 825
18. Shaft from quench-water circulating pump	Water containing 5% solids at 65 C	1 Cr-0.2 Mo-0.4 C steel (LaSalle ETD 150)	Water freezing in pump during shutdown resulting in bent shaft and subsequent fatigue during operation	Protect pump from freezing
IGT U-Gas Pilot Plant				
1. Thermowells and pressure taps (1st failure)	Fluidized char bed and oxidizing gas at max. design temp. of 1065 C	Incoloy 800	Severe sulfidation, embrittlement, and localized melting	Replace with Type 310 or 446 SS
2. Thermowell and pressure tap (2nd failure)	See above	Type 310 SS	Severe sulfidation, oxidation, and localized melting due to excessive operating temperatures	Maintain better temperature control; coat components
3. Internal cyclone dipleg (1st failure)	See above	Incoloy 800	Severe sulfidation and oxidation due to excessive temperatures; some erosive wear	Maintain better temperature control; use Type 310 SS
4. Internal cyclone (1st series of failures)	Low-Btu product gas at 800 to 925 C; particle impingement at 23 to 27 m/s	Type 310 SS, later RA 330 liner and hard-faced RA 330 patch	Perforation of original cyclone and first repair liner by erosion; perforation of second repair at weld line	Use hard-faced RA 330 and avoid welds in high-wear regions
5. Internal cyclone and dipleg (2nd failures)	Fluidized char bed at 1065 C max.; low-Btu product gas at 800 to 925 C	Type 310 SS	Excessive bed height applied cyclic bending moments to assembly, causing separation; dipleg eroded and corroded during immersion in bed	Maintain better bed height and temperature control

TABLE XII (continued)

Component	Operating Environment	Material	Description of Failure	Recommendations
IGT Steam-Iron Pilot Plant				
1. Char preheater off-gas piping	Steam and air with some CO_2, CH_4, and H_2S at 240 C	Type 304 SS	Inter- and transgranular SCC at welds due to sensitization, residual stresses, and corrosive species in steam	Replace with Type 304L SS; stress relieve welds
2. Gas sampling line in reducer	Producer gas at 140 to 195 C; externally insulated and exposed to weather	Type 316 SS asbestos insulation	Transgranular SCC from OD due to chlorides leached from insulation and residual stresses due to cold forming	Use low-chloride insulation; reduce cold forming
Synthane Pilot Plant				
1. Ball-valve stem on coal pretreater feed hopper	Pulverized coal and CO_2 at 149 C	Type 440C SS	Shear fracture of stem due to improper heat treatment and stress concentrations at surface defects	Control heat treatment and surface finish
2. Pipe-to-flange weld in steam-oxygen line	Pressure tested at temperatures to 260 C and pressure to 12 MPa	Types 304 and 316 SS; Type 308 weld	Cracking of weld metal and pipe due to poor welds and SCC from chlorides in city water used for pressure tests	Inspect welds; use deionized water for pressure tests
3. Gasifier heatup line	Steam, CO_2, and combustion gases at 430 C	Type 304 SS	Intergranular SCC from ID near butt weld	Eliminate chlorides
4. Gasifier O_2 line (1st failure)	O_2 at 430 C and 4.1 to 6.9 MPa	Type 304 SS	Transgranular SCC from ID due to chlorides	Eliminate chlorides; use Type 316 SS
5. Gasifier O_2 line (2nd failure)	See above	Type 304L SS	Pitting at ID due to corrosion at surface deposits	Use Type 316 SS; remove deposits
6. Gasifier O_2 line (3rd failure)	See above	Type 304 SS	Leaking at orifice flange due to pitting at ID	See above

TABLE XII (continued)

Component	Operating Environment	Material	Description of Failure	Recommendations
7. Weld-neck flange on gasifier pre-heat line	Steam, at 400 C and 4.1 MPa	Type 304 SS	Intergranular SCC in heat-affected zone near welds assisted by Cl in city water used to backfill loop seal	Use deionized water for backfill
8. Gasifier nozzle	Product gas at 150 to 200 C and 4.1 MPa	Incoloy 800, Monel lined	Leaking crack in heat-affected zone near weld associated with heavy sensitization	Use Monel overlay, C-steel and Incoloy 800 liners
9. Gasifier thermo-well	Product gas at 340 to 400 C and 4.1 MPa	Hastelloy C-276	Severe pitting at OD due to corrosive attack associated with clinker deposition	Reduce thermowell length to prevent clinker formation
10. Distributor-cone thermocouple sheaths	Steam, 0_2, and product gas at 340 to 400 C; combustion products from fuel oil at 540 C during startup	coloy 800	Sulfur from combustion of fuel oil used during startup caused cracking at surface flaws on sheath	Use Type 310 SS; avoid surface flaws and cold work
11. Steam pipe in gasifier	Steam at 400 C and and 4.8 MPa	A335, Grade 1	Ballooning at end of elbow	(cause unknown)
12. Purge pipe inside gasifier	Steam at 430 C at ID, product gas at 430 to 816 C at OD	Inconel 600	Severe pitting and sulfidation attack at OD due to failure to use specified alloy (Incoloy 800)	Replace with Incoloy 800
13. Slurry pump shaft and capscrew	Scrubber recycle water with 15% fines at 230 C; shaft rotates at 3000 rpm	AISI 4140 shaft and AISI 4037 capscrew	Capscrew failed by fatigue due to improper heat treatment and surface defects; resulting eccentric loading of shaft led to fatigue at keyway	Use proper heat treatment, provide fillet on shaft keyway

TABLE XII (continued)

Component	Operating Environment	Material	Description of Failure	Recommendations
Grand Forks Fixed-Bed Slagging-Gasifier Pilot Plant				
1. Gate valve in steam supply system	Deionized water at 93 C and 2.6 to 4.2 MPa	Type 420 SS (Se-doped)	Fracture of valve wedge near connection to stem due to preexisting cracks	Inspect for preexisting flaws
2. Gasifier-vessel vapor barrier liner	Intermittent service over 21 years in raw product gas at temperatures up to 980 C	Type 310 SS	Perforation due to intergranular sulfide attack and sigma-phase formation	None
3. Steam-oxygen injection tuyeres	Internally water cooled; tips contact molten slag at temperatures to 1370 C	Type 347 SS	Severe sulfidation at tips and cracking at weld-metal/base-metal interface	Substitute more sulfidation-resistant alloy; stress relieve after welding
4. Taphole cooling coil	Internally water cooled; OD contacts molten slag at temperatures to 1370 C	Hastelloy G	Intergranular sulfidation cracking from OD, assisted by residual stresses from cold forming	Use Hastelloy C-276; stress relieve after welding
Morgantown Stirred-Bed Gasifier Pilot Plant				
1. Coal bed rabble arm (stirrer)	Internally water cooled; operates in coal bed and oxidizing gas at maximum temperature of 1350 C	Carbon steel	Cracking of welds and adjacent base metal due to high residual stresses; sulfidation attack also present	Stress relieve after welding; consider more sulfidation-resistant alloy
2. External cyclone	Raw product gas at 650 C; char and ash particle impingement at 53 m/s	Hastelloy X	Perforation of wall opposite inlet due to erosive wear	Reduce particle velocities; hard-face critical areas; change inlet design
Westinghouse Coal-Gasification Pilot Plant				
1. Transport line to gasifier vessel	Char fines in product gas at 315 C	SA106, Grade B carbon steel	Severe roughening at ID due to combined erosion/corrosion	Reduce particle velocities; replace with Type 316 SS
Battelle Agglomerating Ash Gasifier Pilot Plant				
1. Char burner thermocouple protection tubes	Coal and calcined bauxite fluidized bed and oxidizing gas at max. temp. of 1230 to 1260 C	Type 446 SS	Severe corrosive attack at OD and cracking of tubes due to clinker deposition at excessively high temperatures	Maintain bed temperature below 1150 C

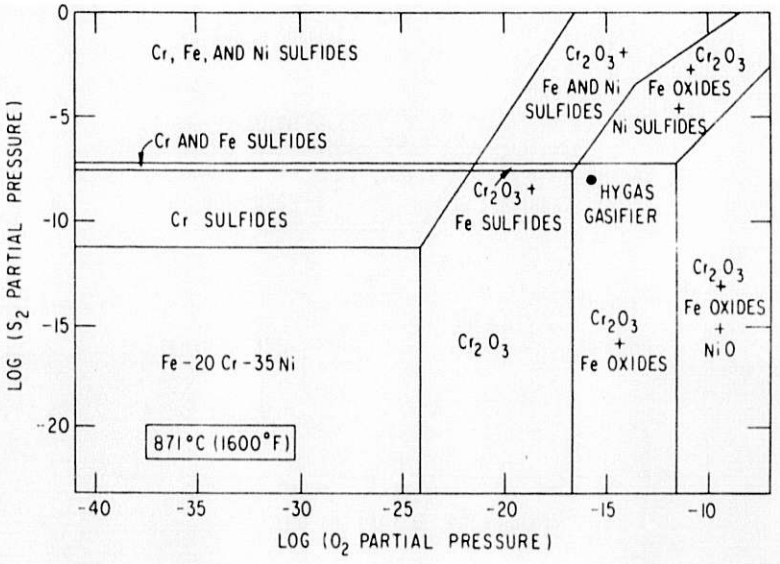

Fig. 19. Thermochemical Diagram at 871°C (1600°F) for an Fe-20Cr-35Ni Alloy.

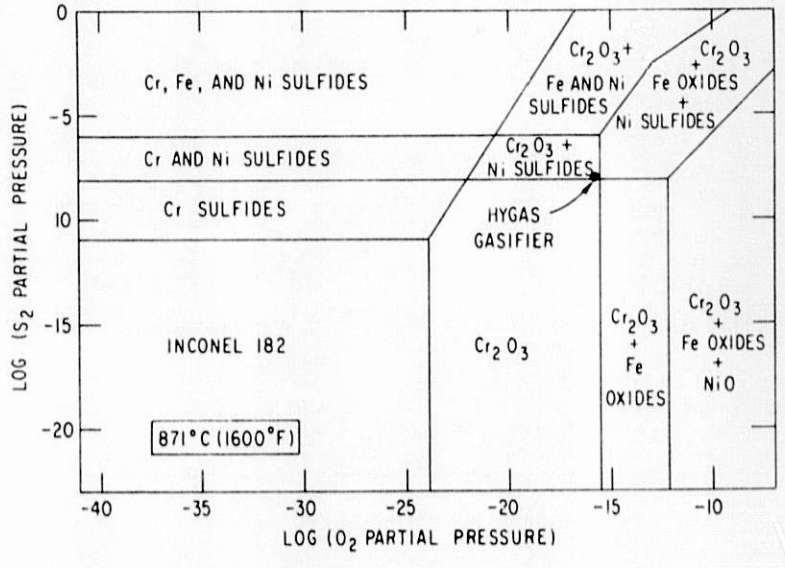

Fig. 20. Simplified Thermochemical Diagram at 871°C (1600°F) for Inconel 182 Weld Metal. Only Fe, Ni, and Cr compounds are shown.

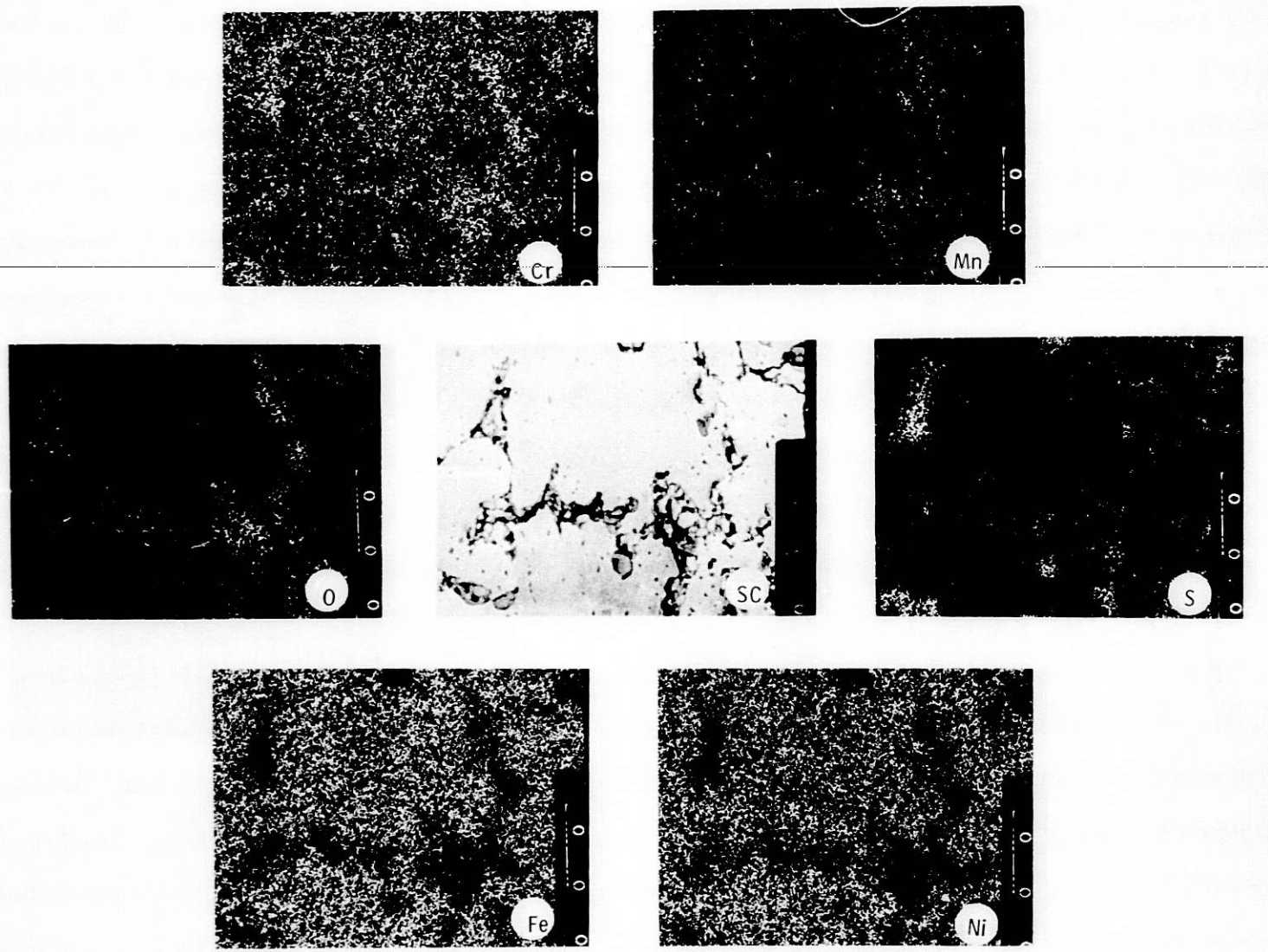

Fig. 21. SEM and Electron Microprobe X-ray Images of Region of Failed Thermocouple Sheath Near ID Surface.

References

1. W.A. Ellingson et al., Materials Technology for Coal-conversion Processes, Progress Report for January-March 1980, Argonne National Laboratory Report ANL-80-46.

2. W.A. Ellingson et al., Materials Technology for Coal-conversion Processes, Nineteenth Report, July-December 1979, Argonne National Laboratory Report ANL-80-12.

3. C.A. Youngdahl, Corrosion Test Coupons - Mechanical Cleaning, Mater. Prot. 5 (10), 53-54 (October 1966).

4. A.N. Jette, M.S. Morris, J.C. Murphy, and J.G. Parker, Active Acoustic Detection of Leaks in Underground Natural Gas Distribution Lines, Mater. Eval. 35 (10), 90-99 (October 1977).

5. T. Claytor, Components Technology Division, Argonne National Laboratory, personal communication.

6. W.C. Reynolds, Computation of Turbulent Flows, Ann. Rev. Fluid Mech. 8, 183-208 (1976).

7. H. Bazerghi and K.J. Serdula, Estimation and Reduction of Errors in Flow Measurements Which Use Cross-correlation Techniques, presented at Mtg. on Reactor Noise, Gatlinburg, TN, 1977.

8. J. Blitz, Fundamentals of Ultrasonics, 2nd Ed., Butterworth, London (1967).

9. P.M. Morse and K.U. Ingard, Theoretical Acoustics, McGraw-Hill, New York (1968).

10. A.V. Karvelis, An Experimental Investigation of the Wall Pressure Fluctuations in Piping Containing Simple Control Devices, Ph.D. thesis, Pennsylvania State University (1975).

11. E.J. Kerschen and J.P. Johnson, Modal Content of Noise Generated by a Coaxial Jet in a Pipe, Stanford University Report MD-38 (1978).

12. D.C. Pridmore-Brown, Sound Propagation in a Fluid Flowing Through an Attenuating Duct, J. Fluid Mech. 4, 393-406 (1958).

13. A.V. Levy, Ed., Proc. Conf. on Corrosion/Erosion of Coal Conversion System Materials, National Association of Corrosion Engineers, Houston, TX (1979).

14. N.R. Baker, C.F. Blazek, and S.R. Tison, Institute of Gas Technology Report ANL/CES/TE79-1 (January 1979).

15. Assessment of Long-term Research Needs for Coal Gasification Technologies, Report of the Fossil Energy Research Working Group, DOE Contract No. ER-78-C-01-6335, MITRE Publishers (April 1979).

References (continued)

16. Synthetic Fuels Data Handbook, 2nd Ed., Cameron Engineers, Inc., Denver, pp. 190-234 (1978).

17. Proc. DOE/EPRI/GRI/NBS 3rd Ann. Conf. on Materials for Coal Conversion and Utilization, Gaithersburg, MD, October 10-12, 1978, CONF-781018.

18. Proc. DOE/EPRI/GRI/NBS 4th Ann. Conf. on Materials for Coal Conversion and Utilization, Gaithersburg, MD, October 9-11, 1979, CONF-791014, pp. II-13 and II-50.

19. K. Natesan, Corrosion and Mechanical Behavior of Materials for Coal-Gasification Applications, Argonne National Laboratory Report ANL-80-5 (May 1980).

20. K. Natesan, High-temperature Corrosion, Prevention of Failures in Coal Conversion Systems, T.R. Shives and W.A. Willard, Eds., NBS Special Publication 468, pp. 159-171 (1977).

21. Clean Fuels from Coal: Symp. II, Institute of Gas Technology, Chicago, IL, June 23-27, 1975, pp. 15-63 and 577-614.

22. Proc. 11th Intersociety Energy Conversion Engineering Congress, 1976, pp. 270-273 and 294-297.

23. W.B. Crouch, W.B. Schlenger, R.D. Klapatch, and G.E. Vitti, Combustion 45, 32-38 (April 1974).

24. O.K. Chopra and K. Natesan, High Temp. Sci. 9, 243-262 (1977).

25. K. Natesan and M.B. Delaplane, Oxidation-Sulfidation Behavior of Materials for Use in Coal-conversion Systems, Corrosion-Erosion Behavior of Materials, K. Natesan, Ed., The Metallurgical Society of AIME, Warrendale, PA, pp. 1-29 (1980).

26. A.J. MacNab, C.F. Braun, and Company, Materials of Construction for High-Btu Coal Gasification Plants, Interim Report, DOE Contract No. EX-76-C-01-2240 (January 1978).

27. W.A. Ellingson et al., Materials Technology for Coal-conversion Processes, Eighteenth Quarterly Report, April-June 1979, Argonne National Laboratory Report ANL-79-93, pp. 1-10.

28. W.A. Ellingson et al., Materials Technology for Coal-conversion Processes, Fourteenth Quarterly Report, April-June 1978, Argonne National Laboratory Report ANL-78-79.

29. D.R. Diercks, Analysis of Failed Transfer Line from the IGT HYGAS Coal Gasification Pilot Plant, to be presented at the Symposium on Material-Environment Interactions in Structural and Pressure Containment Service, 1980 ASME Winter Annual Meeting, Chicago, IL, Nov. 16-21, 1980.

References (continued)

30. S. Danyluk and D.R. Diercks, Failure Analysis Experience with Coal-gasification Pilot Plant Components, to be presented at the Conf. on Properties and Performance of Materials in Coal Gasification Environments, Pittsburgh, PA, Sept. 8-10, 1980.